An implicit non-ordinary state-based peridynamics with stabilised correspondence material model for finite deformation analysis

Nur A. Hashim[a,*], W. M. Coombs[a], C. E. Augarde[a], G. Hattori[b]

[a]*Department of Engineering, Durham University, South Road, DH1 3LE, Durham, UK*
[b]*Department of Engineering, University of Cambridge, Trumpington Street, CB2 1PZ, Cambridge, UK*

Abstract

This paper is devoted to the development of a stabilised implicit non-ordinary state-based peridynamics approach. We propose a geometrically nonlinear implicit approach focusing on quasi-static analyses. Since the construction of the Jacobian matrix is the most time consuming step in conducting this nonlinear analysis, we formulate an analytical expression based on the equation of motion of non-ordinary state-based peridynamics to ensure optimum convergence of the global residual force. The implicit formulation can adopt fairly large time increments, making it a good choice for analyses of finite deformation. Another important extension presented in this paper is the modification of the correspondence material model to remove zero-energy mode instabilities and reduce the spurious oscillations, as proposed by Silling (2017). The derivative of the additional stabilisation term with respect to displacement is included in the formulation of the Jacobian for the first time. Computational examples of 2D finite deformation problems with a stabilised correspondence model are presented. We assess the effectiveness of different values of the stabilisation parameter, G in terms of the particles' spacings and horizon sizes for different problems. This allows the non-ordinary state-based peridynamics approach to model material behaviour with greater accuracy where correspondence materials have previously failed due to instabilities. In this paper, a damage model is also proposed, which provides for the first time an implicit approach for the static solution of crack propagation problems for non-ordinary state-based peridynamics. This paper lays the groundwork for non-ordinary state-based peridynamics to be used for a much greater variety of solid mechanics problems than is currently possible and at the same time satisfying the stability condition.

Keywords: Peridynamics; State-based; Implicit; Finite deformation; Zero-energy mode

*Corresponding author
Email address: nur.a.hashim@durham.ac.uk (Nur A. Hashim)

1. Introduction

Peridynamics (PD) was proposed by Silling [1] as a nonlocal reformulation of the equations of motion to handle solid mechanics problems involving discontinuities. It computes the balance laws in solid mechanics in terms of integro-differential equations and, since no spatial derivatives are required, it permits spontaneously emerged discontinuities without additional remedial techniques [2, 3, 4]. The problem domain is discretised by particles linked through bonds, which contain materials constitutive information. The interaction between particles takes place over a finite distance defined by a horizon, δ. PD is a nonlocal theory and this means that particles separated by a finite distance exert forces upon each other and this interaction extends beyond nearest neighbours. Bond-based peridynamics (BB PD) is the original formulation of PD where the interactions between particles act like spring forces and only depend on the relative displacement of interacting particle pairs [1]. However, the BB PD scheme is restricted to constitutive models with fixed Poisson's ratios: ν of 1/4 for plane strain or 3D problems and 1/3 for plane stress conditions [5, 6].

As a consequence, a plastic incompressibility condition cannot be captured directly with the BB PD [2]. To address this issue, Silling et al. [7] introduced the non-ordinary state-based peridynamics (NOSB PD) formulation as an extension of BB PD to remove the restriction of fixed Poisson's ratios, therefore allowing for the modelling of more complex materials in which particle interactions are defined in terms of force state rather than pairwise force functions [8, 9]. The NOSB PD method leads to more realistic simulations as the forces in the bonds are arrived at by considering the stress and the deformation fields at each of the particles [3, 8, 10, 11, 12, 13, 14, 15, 16, 17, 18, 19, 20, 21, 22, 23, 24], which allows for modelling using general constitutive models.

Numerous advances have been made using PD methods in the past few years including a NOSB PD method proposed by Warren et al. to model deformation and crack propagation in an isotropic bar under quasi-static loading [8]. Foster et al. [9] presented the modelling of explicit dynamic impact tests of aluminium using the NOSB PD formulation. With its unique capability in capturing failure, it is able to simulate crack propagation and damage processes including those in rock-like materials [25] and thermoplastic fracture [16]. The NOSB PD formulation has also been used to model crack growth in an elastic-viscoplastic crystal [26] and in anisotropic materials [20]. However, it is interesting to note that the majority of previous PD research has used explicit time stepping formulations. Two of the rare examples of non-explicit methods are as follows. An implicit NOSB PD formulation was presented in [10] for linearly elastic solids implemented within Emu, a PD code in development at Sandia National Laboratories, and another implicit

implementations of NOSB PD were presented in [27] for crystal plasticity problems and in [28] for the simulation of elastoplasticity within polycrystalline materials. However, the work in [10] was limited to the development and numerical implementation of a small strain linearly elastic material model. In reference [27] the computation of tangent modulus was based on the crystal plasticity constitutive model. A conference paper has previously mentioned implicit NOSB PD but not enough detail was given about the implementation [29].

Fracture modelling was the focus of early research in PD, utilizing simple constitutive models as stated in [30]. NOSB PD as a nonlocal meshless method is not limited in the amount of deformation since there are no mesh regularity constraints to consider and this has been relatively unexplored in the literature. The PD method has been widely used to solve quasi-static problems [8, 31, 32, 27, 33, 34, 35, 22]. However as mentioned earlier, the most common PD approaches are based on explicit time integration schemes and a drawback arises from the limitation on the time step size to ensure numerical stability and in the case of quasi-static loading, it becomes expensive to obtain solutions.

Recently there have been initial attempts to include material damage and failure for PD with implicit solution procedures. Tao Ni et al. [36] introduces two implicit static solution procedures and this has been implemented in BB PD. The most frequently used constitutive model in PD is the Prototype Microelastic Brittle (PMB) material proposed by Silling and Askari [3] for which when a bond fails, its strength and stiffness suddenly drop to zero. However, the discontinuity of the constitutive law prevents a standard implementation of a Newton-Raphson type of algorithm as stated in [36]. In this work, damage will be included for the first time within a NOSB PD approach with an implicit solution scheme based on the Newton-Raphson (NR) solution procedure.

One of the particular drawbacks of NOSB PD is an instability problem which leads to spurious zero-energy modes, as previously identified in the mathematical formulation of the PD theory [13, 10, 37, 38, 18, 21, 19]. Zero-energy modes have been overcome in the classical Finite Element Method (FEM) by inserting artificial stiffness to increase stability [39]. Littlewood [26] and Breitenfeld et al. [10] working with PD methods provided different forms of an additional term to the PD force vector state which represents the supplemental bond between particles, resembling the method used in the FEM. A stabilised displacement field was introduced by Wu and Ren [13] to control the zero-energy mode while Yaghoobi and Chorzepa proposed calculation of the deformation gradient based on higher-order polynomial approximation which is viable in enhancing the accuracy of the method with larger horizons [18]. Recently, Silling has introduced

a stabilised "correspondence" material model which satisfies the stability condition [37]. To the best of the authors' knowledge, this stabilised correspondence material model has not been studied in the context of the elimination of zero-energy modes for finite deformation or implicit NOSB PD. In the literature, further approaches have been suggested [21, 19], which are generalisations of [37]. [40] introduced a method to minimize the non-uniform deformation state and is similar to the stabilisation scheme recently proposed in [37] . The convergence and accuracy of [40]'s approach is further demonstrated in [41].

In this paper, an implicit NOSB PD method for nonlinear quasi-static problems with finite deformation is presented for the first time. Although implicit approaches are more complex and harder to implement, the advantages of the proposed implicit approach include allowance of much larger time steps, giving benefit in terms of computational runtime, especially for large deformation problems. Moreover, this paper assesses the accuracy of the proposed stabilised NOSB PD framework with the correspondence material model [37] and demonstrates it for 2D elastic large deformation problems. This paper consists of four main technical elements. Firstly, the numerical implementations are derived within a finite deformation framework. Based on this, the Jacobian matrices of the NOSB PD with a correspondence continuum model for both the unstabilised and stabilised versions [37] are developed. The accuracy is assessed with the inclusion of different stabilisation parameters. Finally, this paper introduces an implicit approach for crack propagation problems in NOSB PD. It is to be noted that the implicit non-ordinary state-based formulation is implemented in a Matlab code.

2. Non-ordinary state-based peridynamics theory with finite deformation framework

PD formulations can be classified into bond-based (BB PD) and state-based peridynamics (SB PD). The SB PD formulations can be further categorised as ordinary state-based peridynamics (OSB PD) and non-ordinary state-based peridynamics (NOSB PD) depending on the modelling of the force term. In the BB PD, the forces, $\mathbf{f}$, between two particles ($\mathbf{x}$ and $\mathbf{x}'$) always have equal magnitude and opposite directions, thus conserving linear and angular momentum. On the other hand, in the OSB PD formulation, the forces in the bonds, $\underline{\mathbf{T}}$ and $\underline{\mathbf{T}}'$ defined as the force vector states, are aligned in the direction of the bonds, as in the bond-based approach but do not need to have equal magnitudes. The conservation of angular momentum is satisfied in the OSB PD formulation, whereas in the NOSB PD formulation, the force states place no restriction on the magnitude and direction of forces. [7]. These differences are illustrated in Fig. 1. The

force densities, $\mathbf{t}$ and $\mathbf{t}'$ are expressed as

$$\mathbf{t} = \underline{\mathbf{T}}(\mathbf{x})\langle \mathbf{x}' - \mathbf{x} \rangle \quad \text{and} \quad \mathbf{t}' = \underline{\mathbf{T}}(\mathbf{x}')\langle \mathbf{x} - \mathbf{x}' \rangle, \tag{1}$$

extracted by the force states operating on the corresponding relative position vectors.

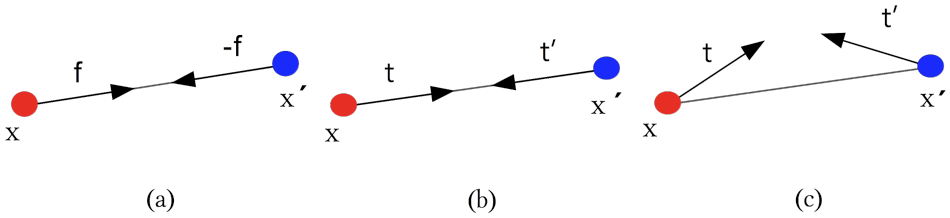

Fig. 1. Illustration of the tractions in the PD bonds in (a) BB PD, (b) OSB PD and (c) NOSB PD.

2.1. Finite deformation

The deformation gradient is the fundamental quantity for measuring deformation in continuum mechanics. The deformation gradient characterises the deformation in the neighbourhood of a particle and is defined as

$$\mathbf{F} = \frac{\partial \mathbf{y}}{\partial \mathbf{x}}, \tag{2}$$

where $\mathbf{y}$ denotes a particle in the deformed configuration, while $\mathbf{x}$ denotes the same particle in the reference configuration. In accordance with the polar decomposition theorem, the deformation gradient allows the deformation from an initial state to a deformed configurations to be split into a sequence of configuration as shown in Fig. 2 where

$$\mathbf{F} = \mathbf{RU} = \mathbf{VR}, \tag{3}$$

where $\mathbf{R}$ is an orthogonal tensor representing pure rotation, and $\mathbf{U}$ and $\mathbf{V}$ are symmetric right and left stretch tensors, respectively. Moreover, the right and left Cauchy-Green deformation tensors are defined as

$$\mathbf{C} = \mathbf{U}^2 = \mathbf{F}^T\mathbf{F}, \quad \mathbf{c} = \mathbf{V}^2 = \mathbf{F}\mathbf{F}^T. \tag{4}$$

In this paper, logarithmic (Hencky) strain is used to measure the large deformations of materials with the Hencky hyperelasticity assumption (a linear relationship between Kirchhoff stress and logarithmic strain). A linear hyperelastic relationship between Kirchhoff stress and logarithmic strains has been found to be an

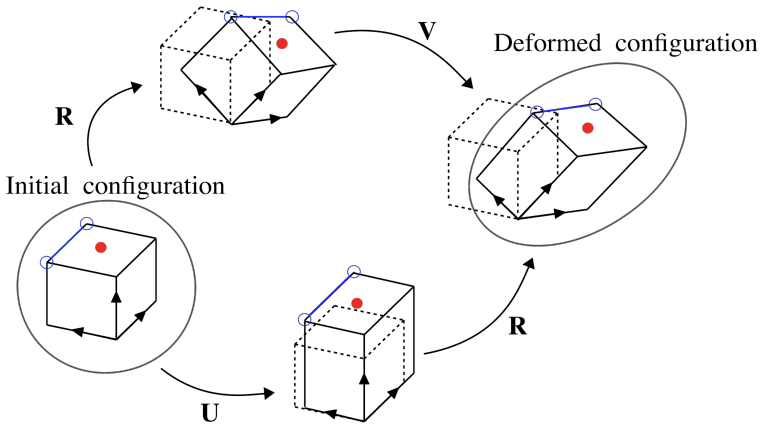

Fig. 2. Illustration of the polar decomposition of the deformation gradient.

accurate representation if the elastic strains are moderately large [42]. The Hencky strain is defined as

$$\boldsymbol{\epsilon} = \ln(\mathbf{c}), \tag{5}$$

and the Kirchhoff stress is then given by

$$\tau = \mathbf{D}^e \boldsymbol{\epsilon}, \tag{6}$$

where $\mathbf{D}^e$ is the fourth order linear elastic isotropic material stiffness tensor. The Cauchy stress tensor can be expressed as

$$\boldsymbol{\sigma} = \frac{\boldsymbol{\tau}}{J}, \tag{7}$$

where the stress tensors are related by the volumetric ratio, J between the deformed and reference configurations, given by the determinant of the deformation gradient

$$J = \det \mathbf{F}. \tag{8}$$

2.2. Non-ordinary state-based peridynamics for quasi-static analysis

Based on the principle of virtual work, the equation of motion of NOSB PD takes the following form [7]

$$\mathbf{L} + \mathbf{b} = \rho \ddot{\mathbf{u}}, \tag{9}$$

where the internal force vector at particle $\mathbf{x}$ is

$$\mathbf{L}[\mathbf{x}, t] = \int_R \left\{ \underline{\mathbf{T}}[\mathbf{x}, t]\langle \mathbf{x}' - \mathbf{x} \rangle - \underline{\mathbf{T}}[\mathbf{x}', t]\langle \mathbf{x} - \mathbf{x}' \rangle \right\} dV_{\mathbf{x}'}, \tag{10}$$

in which ρ represents the mass density in the initial configuration, $\ddot{\mathbf{u}}$ is the second-order time derivative of displacement $\mathbf{u}$, $\mathbf{b}$ is the body force at time t, and $\underline{\mathbf{T}}\,[\mathbf{x}, t]\langle \mathbf{x}' - \mathbf{x}\rangle$ is the force vector state. The angle brackets $\langle\ \rangle$ denotes the vector mapped by the force vector state originating at the particle in square brackets [ ]. The $\mathbf{L}[\mathbf{x}, t]$ depends not only on the deformation of all bonds connected to particle $\mathbf{x}$ but also on the deformation of all bonds connected to particle $\mathbf{x}'$. $V_{\mathbf{x}'}$ is the volume associated with particle $\mathbf{x}'$. A kinematic illustration of NOSB PD is shown in Fig. 3 where R is a circular neighbourhood of given radius with δ centered at particle $\mathbf{x}$. The reference position vector state between two particles is denoted by $\boldsymbol{\xi} = \mathbf{x}' - \mathbf{x}$ and the relative displacement by $\boldsymbol{\eta} = \mathbf{u}' - \mathbf{u}$. Using those definitions, the deformation vector state, $\underline{\mathbf{Y}}$ denotes the deformed state of the bond where $\mathbf{y}$ and $\mathbf{y}'$ are shown after a displacement has been imposed on particles $\mathbf{x}$ and $\mathbf{x}'$ respectively. The equation of motion in the NOSB PD, Eq. (9) and the integral expression in Eq. (10) can be approximated with a finite sum as

$$\Big(\sum_{j=1}^{m} \underline{\mathbf{T}}\,[\mathbf{x}_i, t]\langle \mathbf{x}_j - \mathbf{x}_i\rangle - \underline{\mathbf{T}}\,[\mathbf{x}_j, t]\langle \mathbf{x}_i - \mathbf{x}_j\rangle\Big) V_j + \mathbf{b}(\mathbf{x}_i, t) = \rho(\mathbf{x}_i)\ddot{\mathbf{u}}(\mathbf{x}_i, t), \tag{11}$$

where j is a counter for the m particles in the horizon of particle i and V_j is the volume of particle j in reference configuration. The PD force vector state of the bond vector $\boldsymbol{\xi}$ can be obtained from the first Piola-Kirchhoff stress tensor as [8]

$$\underline{\mathbf{T}}\,[\mathbf{x}, t]\langle \mathbf{x}' - \mathbf{x}\rangle = \omega\langle \boldsymbol{\xi}\rangle \mathbf{P}(\mathbf{x})^T \mathbf{B}(\mathbf{x})\,\boldsymbol{\xi}, \tag{12}$$

where the first Piola-Kirchhoff stress, $\mathbf{P}(\mathbf{x})$, for each particle $\mathbf{x}$ can be obtained from the Cauchy stress, $\boldsymbol{\sigma}$, and the deformation gradient, $\mathbf{F}(\mathbf{x})$, as

$$\mathbf{P}(\mathbf{x}) = J\boldsymbol{\sigma}(\mathbf{x})\mathbf{F}(\mathbf{x})^{-T}. \tag{13}$$

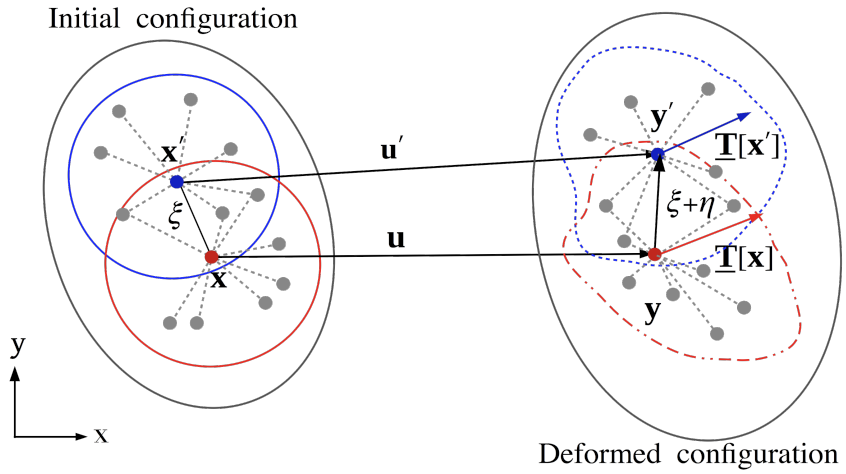

Fig. 3. Kinematic illustration of NOSB PD in 2D.

In (12), $\omega\langle\boldsymbol{\xi}\rangle$ is a dimensionless non-negative weighting function of radius δ in the reference frame, that defines the horizon in which the nonlocal interactions take place. In this work, consistent with [8], a constant weighing function is adopted, that is

$$\omega\langle\boldsymbol{\xi}\rangle = \begin{cases} 1 & \text{if } \boldsymbol{\xi} \leq \delta, \\ 0 & \text{if } \boldsymbol{\xi} > \delta. \end{cases} \tag{14}$$

$\mathbf{B}(\mathbf{x})$ is referred to as the nonlocal shape tensor and is dependent on the orientation of the bonds in the reference configuration and

$$\mathbf{B}(\mathbf{x}) = \int_R \omega\langle\boldsymbol{\xi}\rangle(\boldsymbol{\xi} \otimes \boldsymbol{\xi}) dV_{\boldsymbol{\xi}}, \tag{15}$$

where $\otimes$ denotes the dyadic product of two vectors. The nonlocal PD deformation gradient is expressed as a nonlocal integration given by [7]

$$\mathbf{F}(\mathbf{x}) = \left(\int_R \omega\langle\boldsymbol{\xi}\rangle(\underline{\mathbf{Y}}(\boldsymbol{\xi}) \otimes \boldsymbol{\xi}) dV_{\boldsymbol{\xi}} \right) \mathbf{B}(\mathbf{x})^{-1}. \tag{16}$$

For a discrete system, the shape tensor in Eq. (15) at particle i can be expressed as a Riemann sum in matrix form as

$$\mathbf{B}(\mathbf{x}_i) = \begin{bmatrix} \sum_{j=1}^{m} \omega\langle\boldsymbol{\xi}\rangle(\xi_x\xi_x)V_j & \sum_{j=1}^{m} \omega\langle\boldsymbol{\xi}\rangle(\xi_x\xi_y)V_j \\ \sum_{j=1}^{m} \omega\langle\boldsymbol{\xi}\rangle(\xi_y\xi_x)V_j & \sum_{j=1}^{m} \omega\langle\boldsymbol{\xi}\rangle(\xi_y\xi_y)V_j \end{bmatrix}, \tag{17}$$

and the nonlocal deformation gradient in Eq. (16) as

$$\mathbf{F}(\mathbf{x}_i) = \begin{bmatrix} \sum_{j=1}^{m} \omega\langle\boldsymbol{\xi}\rangle(\underline{Y}(\xi_x)\xi_x)V_j & \sum_{j=1}^{m} \omega\langle\boldsymbol{\xi}\rangle(\underline{Y}(\xi_x)\xi_y)V_j \\ \sum_{j=1}^{m} \omega\langle\boldsymbol{\xi}\rangle(\underline{Y}(\xi_y)\xi_x)V_j & \sum_{j=1}^{m} \omega\langle\boldsymbol{\xi}\rangle(\underline{Y}(\xi_y)\xi_y)V_j \end{bmatrix} \mathbf{B}(\mathbf{x}_i)^{-1}. \tag{18}$$

The governing equation for quasi-static analysis is obtained by setting the acceleration term in Eq. (11) to zero, i.e.

$$\Big(\sum_{j=1}^{m} \underline{\mathbf{T}}\,[\mathbf{x}_i, t]\langle\mathbf{x}_j - \mathbf{x}_i\rangle - \underline{\mathbf{T}}\,[\mathbf{x}_j, t]\langle\mathbf{x}_i - \mathbf{x}_j\rangle \Big) V_j + \mathbf{b}(\mathbf{x}_i, t) = 0. \tag{19}$$

Substituting Eq. (12) into Eq. (19), the quasi-static equations of motion in NOSB PD can be expressed as

$$\Big(\sum_{j=1}^{m} \omega_i\langle\boldsymbol{\xi}\rangle\mathbf{P}(\mathbf{x}_i)^T\mathbf{B}(\mathbf{x}_i)\,\boldsymbol{\xi}_i - \omega_j\langle\boldsymbol{\xi}\rangle\mathbf{P}(\mathbf{x}_j)^T\mathbf{B}(\mathbf{x}_j)\,\boldsymbol{\xi}_j \Big) V_j + \mathbf{b}(\mathbf{x}_i, t) = 0. \tag{20}$$

3. Numerical implementation

In general, time integration schemes are divided into two categories: explicit and implicit where the former are usually simpler to implement than the latter. However, due to the nature of explicit time integration, which is only conditionally stable and requires small time steps, obtaining solutions under quasi-static conditions involving large deformations becomes expensive. In these situations, implicit methods have the potential to be more computationally efficient and accurate compared to explicit methods. In this section, we provide a detailed implementation of a geometrically nonlinear implicit NOSB PD method.

3.1. Newton-Raphson procedure

In this paper, we utilise a full Newton-Raphson (NR) method in order to solve the nonlinear system of equations and update the Jacobian matrix at each iteration. The Jacobian matrix is recomputed at each iteration thus enabling convergence at a higher rate than other alternatives [43]. Imposed loads are applied in increments and within each increment, force equilibrium is sought between internal resisting forces and external forces, resulting in the following expression that needs to be satisfied

$$\mathbf{f}^{int}(\mathbf{u}) - \mathbf{f}^{ext} = 0, \tag{21}$$

where $\mathbf{f}^{int}$ is the internal force and $\mathbf{f}^{ext}$ is the external force, where from Eq. (20)

$$\mathbf{f}^{int} = \Big(\sum_{j=1}^{m} \omega_i\langle\boldsymbol{\xi}\rangle\mathbf{P}(\mathbf{x}_i)^T\mathbf{B}(\mathbf{x}_i)\,\boldsymbol{\xi}_i - \omega_j\langle\boldsymbol{\xi}\rangle\mathbf{P}(\mathbf{x}_j)^T\mathbf{B}(\mathbf{x}_j)\,\boldsymbol{\xi}_j \Big) V_j \quad \text{and} \quad \mathbf{f}^{ext} = -\mathbf{b}(\mathbf{x}_i, t). \tag{22}$$

The solution of this nonlinear system of equations can be obtained from repeatedly solving a linear system

$$\mathbf{K}(\triangle \mathbf{u}_{l+1}) = \mathbf{f}_l^{oobf}, \tag{23}$$

where l+1 represent the current equilibrium iteration within the NR procedure and $\mathbf{f}^{oobf}$ = $\mathbf{f}^{ext}$- $\mathbf{f}^{int}$ is the global residual or out of balance force vector for the current displacements. $\mathbf{K}$ is the Jacobian matrix where

$$\mathbf{K} = \frac{\partial \mathbf{f}^{int}}{\partial u} = \begin{bmatrix} \frac{\partial \mathbf{f}_1^{int}}{\partial u_1} & \frac{\partial \mathbf{f}_1^{int}}{\partial u_2} & \cdots & \frac{\partial \mathbf{f}_1^{int}}{\partial u_{ndof}} \\ \frac{\partial \mathbf{f}_2^{int}}{\partial u_1} & \frac{\partial \mathbf{f}_2^{int}}{\partial u_2} & \cdots & \frac{\partial \mathbf{f}_2^{int}}{\partial u_{ndof}} \\ \vdots & \vdots & \ddots & \vdots \\ \frac{\partial \mathbf{f}_{ndof}^{int}}{\partial u_1} & \frac{\partial \mathbf{f}_{ndof}^{int}}{\partial u_2} & \cdots & \frac{\partial \mathbf{f}_{ndof}^{int}}{\partial u_{ndof}} \end{bmatrix}, \tag{24}$$

with $ndof$ the total number of degrees of freedom in the system. The out of balance force needs to be evaluated in order to verify if the system is in equilibrium. The incremental displacement is equivalent to the summation of the increment in displacement within the current loadstep, that is

$$\mathbf{u}_{n+1} = \mathbf{u}_n + \sum_{l=1}^{n_{NRit}} \triangle \mathbf{u}_l, \tag{25}$$

where n+1 represents the current loadstep and n_{NRit} is the total number of NR iterations. The NR procedure is performed until the convergence criterion is attained, such that

$$\frac{|\mathbf{f}^{oobf}|}{|\mathbf{f}^{ext}|} \leq tol, \tag{26}$$

where tol is the prescribed relative error tolerance (1×10^{-10} is used in this paper). The analysis proceeds with the next loadstep once the NR process obtain a converged solution to within the specified tolerance. It is to be noted that direct solver with backslash command were used for the matrix solution.

3.2. Jacobian matrix

The Jacobian matrix or so-called tangent stiffness matrix can be constructed via analytical and numerical approaches. It is not feasible to compute the tangent stiffness matrix numerically due to the high computational time and high memory requirement. We determine an analytical expression as follows

$$\mathbf{K} = \sum_{i}^{I_n} \sum_{j=1}^{m} \sum_{k}^{ndof} \left(\omega_i(|\boldsymbol{\xi}|) \frac{\partial \underline{\mathbf{T}}[\mathbf{x}_i]}{\partial \mathbf{u}_k} \right) - \left(\omega_j(|\boldsymbol{\xi}|) \frac{\partial \underline{\mathbf{T}}[\mathbf{x}_j]}{\partial \mathbf{u}_k} \right), \tag{27}$$

which can be expressed in matrix form as

$$\mathbf{K} = \begin{bmatrix} \frac{\sum_{j=1}^{m}\left(\omega_1(|\underline{\boldsymbol{\xi}}|)\partial\underline{\mathbf{T}}[\mathbf{x}_1]\right)-\left(\omega_j(|\underline{\boldsymbol{\xi}}|)\partial\underline{\mathbf{T}}[\mathbf{x}_j]\right)}{\partial u_1} & \frac{\sum_{j=1}^{m}\left(\omega_1(|\underline{\boldsymbol{\xi}}|)\partial\underline{\mathbf{T}}[\mathbf{x}_1]\right)-\left(\omega_j(|\underline{\boldsymbol{\xi}}|)\partial\underline{\mathbf{T}}[\mathbf{x}_j]\right)}{\partial u_2} & \cdots & \frac{\sum_{j=1}^{m}\left(\omega_1(|\underline{\boldsymbol{\xi}}|)\partial\underline{\mathbf{T}}[\mathbf{x}_1]\right)-\left(\omega_j(|\underline{\boldsymbol{\xi}}|)\partial\underline{\mathbf{T}}[\mathbf{x}_j]\right)}{\partial u_{ndof}} \\ \frac{\sum_{j=1}^{m}\left(\omega_2(|\underline{\boldsymbol{\xi}}|)\partial\underline{\mathbf{T}}[\mathbf{x}_2]\right)-\left(\omega_j(|\underline{\boldsymbol{\xi}}|)\partial\underline{\mathbf{T}}[\mathbf{x}_j]\right)}{\partial u_1} & \frac{\sum_{j=1}^{m}\left(\omega_2(|\underline{\boldsymbol{\xi}}|)\partial\underline{\mathbf{T}}[\mathbf{x}_2]\right)-\left(\omega_j(|\underline{\boldsymbol{\xi}}|)\partial\underline{\mathbf{T}}[\mathbf{x}_j]\right)}{\partial u_2} & \cdots & \frac{\sum_{j=1}^{m}\left(\omega_2(|\underline{\boldsymbol{\xi}}|)\partial\underline{\mathbf{T}}[\mathbf{x}_2]\right)-\left(\omega_j(|\underline{\boldsymbol{\xi}}|)\partial\underline{\mathbf{T}}[\mathbf{x}_j]\right)}{\partial u_{ndof}} \\ \vdots & \vdots & \ddots & \vdots \\ \frac{\sum_{j=1}^{m}\left(\omega_{I_n}(|\underline{\boldsymbol{\xi}}|)\partial\underline{\mathbf{T}}[\mathbf{x}_{I_n}]\right)-\left(\omega_j(|\underline{\boldsymbol{\xi}}|)\partial\underline{\mathbf{T}}[\mathbf{x}_j]\right)}{\partial u_1} & \frac{\sum_{j=1}^{m}\left(\omega_{I_n}(|\underline{\boldsymbol{\xi}}|)\partial\underline{\mathbf{T}}[\mathbf{x}_{I_n}]\right)-\left(\omega_j(|\underline{\boldsymbol{\xi}}|)\partial\underline{\mathbf{T}}[\mathbf{x}_j]\right)}{\partial u_2} & \cdots & \frac{\sum_{j=1}^{m}\left(\omega_{I_n}(|\underline{\boldsymbol{\xi}}|)\partial\underline{\mathbf{T}}[\mathbf{x}_{I_n}]\right)-\left(\omega_j(|\underline{\boldsymbol{\xi}}|)\partial\underline{\mathbf{T}}[\mathbf{x}_j]\right)}{\partial u_{ndof}} \end{bmatrix}. \tag{28}$$

Substituting Eq. (12) into Eq. (27), the Jacobian can be expressed as

$$\mathbf{K} = \sum_{i}^{I_n}\sum_{j=1}^{m}\sum_{k}^{ndof}\left(\omega_i(|\boldsymbol{\xi}|)\frac{\partial\mathbf{P}_i}{\partial\mathbf{F}_i}\frac{\partial\mathbf{F}_i}{\partial\mathbf{u}_k}\mathbf{B}_i\left(\mathbf{x}_j-\mathbf{x}_i\right)\right)-\left(\omega_j(|\boldsymbol{\xi}|)\frac{\partial\mathbf{P}_j}{\partial\mathbf{F}_j}\frac{\partial\mathbf{F}_j}{\partial\mathbf{u}_k}\mathbf{B}_j\left(\mathbf{x}_i-\mathbf{x}_j\right)\right)V_j. \tag{29}$$

Note that only the particles related to particle $\mathbf{x}_i$ and $\mathbf{x}_j$ contribute to the the row of the Jacobian matrix corresponding to particle $\mathbf{x}_i$. For this reason, the matrix sparsity depends on the horizon size, δ. I_n is the total number of particles and therefore, for a 2D problem, the global matrix size is $2I_n \times 2I_n$. The algorithmic PD calculation sequence for the finite deformation formulation is given in Fig. 4, where i denotes the particle, j is a counter for the m particles in the horizon of particle i and k is a counter for the $ndof$ degrees of freedom. The nonlocal shape tensor and deformation gradient is approximated for each individual particle from which nonlocal values can be obtained for the elastic Cauchy-Green strain $\mathbf{c}(\mathbf{x})$, logarithmic elastic strain $\boldsymbol{\epsilon}(\mathbf{x})$, Kirchhoff stress $\boldsymbol{\tau}(\mathbf{x})$ and first Piola-Kirchhoff stress $\mathbf{P}(\mathbf{x})$ before the NOSB PD force vector state functions for each bond at a particle can be obtained. In order to construct the Jacobian matrix in Eq. (29), we need to determine the derivative of the first Piola-Kirchhoff stress with respect to the deformation gradient and the derivative of the deformation gradient with respect to the displacement. The derivative of the first Piola-Kirchhoff stress with respect to the deformation gradient can be expressed as

$$\begin{aligned} \mathbf{A} &= \frac{\partial\mathbf{P}}{\partial\mathbf{F}} \\ &= \frac{\partial\boldsymbol{\tau}}{\partial\mathbf{F}}\mathbf{F}^{-T} + \boldsymbol{\tau}\frac{\partial\mathbf{F}^{-T}}{\partial\mathbf{F}}, \end{aligned} \tag{30}$$

where $\mathbf{A}$ denotes the material tangent modulus, often referred to as the first elasticity tensor for materials with an elastic constitutive law. For the sake of brevity, the complete derivation of $\mathbf{A}$ is not included here (see Appendix A for the full derivation). Combining the derivative of the Kirchhoff stress with respect to the elastic logarithmic strain tensor, $\mathbf{Q}$, the stiffness matrix for isotropic linear elasticity, $\mathbf{D}^e$ and the derivative of the Cauchy-Green strain with respect to the deformation gradient, $\mathbf{N}$, we obtain the follow equation for

the spatial tangent stiffness matrix, $\mathbf{M}$ where

$$\mathbf{M} = \mathbf{Q}\mathbf{D}^{e}\mathbf{N}, \tag{31}$$

$$\mathbf{Q} = \frac{\partial \boldsymbol{\epsilon}}{\partial \mathbf{c}} = \frac{1}{2}\frac{\partial ln(\mathbf{c})}{\partial \mathbf{c}}, \tag{32}$$

and

$$\mathbf{N} = \frac{\partial \mathbf{c}}{\partial \mathbf{F}}. \tag{33}$$

Forming this $\mathbf{M}$ matrix, we obtain $\mathbf{A}$. Turning our focus to the formulation of the derivative of the deformation gradient with respect to the displacement in Eq. (29), we obtain

$$\mathbf{H} = \frac{\partial \mathbf{F}}{\partial \mathbf{u}_k} = \begin{bmatrix} \sum_{j=1}^{m} \omega\langle\boldsymbol{\xi}\rangle(\frac{\partial \underline{Y}(\xi_x)}{\partial \mathbf{u}_k})\xi_x V_j & \sum_{j=1}^{m} \omega\langle\boldsymbol{\xi}\rangle(\frac{\partial \underline{Y}(\xi_x)}{\partial \mathbf{u}_k})\xi_y V_j \\ \sum_{j=1}^{m} \omega\langle\boldsymbol{\xi}\rangle(\frac{\partial \underline{Y}(\xi_y)}{\partial \mathbf{u}_k})\xi_x V_j & \sum_{j=1}^{m} \omega\langle\boldsymbol{\xi}\rangle(\frac{\partial \underline{Y}(\xi_y)}{\partial \mathbf{u}_k})\xi_y V_j \end{bmatrix} \mathbf{B}^{-1}. \tag{34}$$

Substituting Eq. (34) and Eq. (30) into Eq. (27) leads to the construction of the global tangent stiffness as shown in Fig. 4.

3.3. Stabilised non-ordinary peridynamics

So-called correspondence material models allow a material model from standard local theory to model long-range forces with the inherent capabilities of nonlocal PD formulation. However, in a uniform particle discretisation, correspondence models suffer from instability due to zero-energy modes. In the context of the NOSB PD formulation, the spurious zero-energy modes are attributed to the weak couplings between particles within a horizon and this causes stability issues which have been reported in [10, 38, 13, 18]. In the presence of zero-energy modes, simulations exhibit oscillations in the deformation and stress fields. This is caused by the missing role of the centre particle when approximating the deformation gradient tensor and all correspondence materials fail this stability condition [37]. In order to understand its origin, imagine a

i	1	2	I_n	FOR EACH Particle		
j	1	2	$....m$	FOR EACH Neighbouring Particle		
$\mathbf{B}$				shape tensor END FOR	$\mathbf{B}(\mathbf{x}_i) = \sum_{j=1}^{m} \omega\langle\boldsymbol{\xi}\rangle(\boldsymbol{\xi}\otimes\boldsymbol{\xi})V_j$	(15)
j	1	2	$....m$	FOR EACH Neighbouring Particle		
$\mathbf{F}$				deformation gradient tensor END FOR	$\mathbf{F}(\mathbf{x}_i) = (\sum_{j=1}^{m} \omega\langle\boldsymbol{\xi}\rangle(\underline{Y}(\boldsymbol{\xi})\otimes\boldsymbol{\xi})V_j)\mathbf{B}(\mathbf{x}_i)^{-1}$	(16)
$\mathbf{b}^e$				elastic left Cauchy-Green strain	$\mathbf{c}(\mathbf{x}_i) = \mathbf{F}(\mathbf{x}_i)\mathbf{F}(\mathbf{x}_i)^T$	
$\boldsymbol{\epsilon}$				logarithmic elastic strain	$\boldsymbol{\epsilon}(\mathbf{x}_i) = \frac{1}{2}\log(\mathbf{c})$	(5)
$\boldsymbol{\tau}$				Kirchhoff stress	$\boldsymbol{\tau}(\mathbf{x}_i) = \mathbf{D}^e\boldsymbol{\epsilon}(\mathbf{x}_i)$	(6)
$\mathbf{P}$				first Piola-Kirchhoff stress	$\mathbf{P}(\mathbf{x}_i) = \boldsymbol{\tau}(\mathbf{x}_i)\mathbf{F}(\mathbf{x}_i)^{-T}$	(13)
$\underline{\mathbf{T}}$				force vector state	$\underline{\mathbf{T}}(\mathbf{x}_i) = \omega\langle\boldsymbol{\xi}\rangle\mathbf{P}(\mathbf{x}_i)^T\mathbf{B}\,\boldsymbol{\xi}$	(12)
j	1	2	$....m$	FOR EACH Neighbouring Particle		
$\mathbf{L}$				particle internal force END FOR	$\mathbf{L}(\mathbf{x}_i) = \sum_{j=1}^{m}(\underline{\mathbf{T}}[\mathbf{x}_i, t] - \underline{\mathbf{T}}[\mathbf{x}_j, t])V_j$	(10)
$\mathbf{Q}$				derivative of logarithmic elastic strain with respect to the left Cauchy-Green strain	$\mathbf{Q}(\mathbf{x}_i) = \frac{1}{2}\frac{\partial \ln\mathbf{c}(\mathbf{x}_i)}{\partial \mathbf{c}(\mathbf{x}_i)}$	(A.3)
$\mathbf{N}$				derivative of Cauchy-Green strain with respect to the deformation gradient	$\mathbf{N}(\mathbf{x}_i) = \frac{\partial \mathbf{c}(\mathbf{x}_i)}{\partial \mathbf{F}(\mathbf{x}_i)}$	(A.5)
$\mathbf{M}$				spatial tangent stiffness matrix	$\mathbf{M}(\mathbf{x}_i) = \mathbf{D}^e\mathbf{Q}(\mathbf{x}_i)\mathbf{N}(\mathbf{x}_i)$	(31)
$\mathbf{A}$				derivative of Piola-Kirchhoff with respect to the deformation gradient	$\mathbf{A}(\mathbf{x}_i) = \frac{\partial(\boldsymbol{\tau}\mathbf{F}^{-T}(\mathbf{x}_i))}{\partial \mathbf{F}(\mathbf{x}_i)}$	(30)
$\mathbf{H}$				derivative of deformation gradient with respect to the displacement	$\mathbf{H}(\mathbf{x}_i) = \sum_{j=1}^{m} \omega\langle\boldsymbol{\xi}\rangle\left(\frac{\partial \underline{Y}(\boldsymbol{\xi})}{\partial u}\otimes\boldsymbol{\xi}\right)V_j$	(29)
k	1	2	$....ndof$	FOR EACH Degree of freedom		
$\mathbf{K}$				END FOR	$\mathbf{K} = \sum_{k}^{ndof}\left(\omega_i(\lvert\boldsymbol{\xi}\rvert)\frac{\partial \underline{\mathbf{T}}[\mathbf{x}_i]}{\partial \mathbf{u}_k}\right) - \left(\omega_j\langle\boldsymbol{\xi}\rangle\frac{\partial \underline{\mathbf{T}}[\mathbf{x}_j]}{\partial \mathbf{u}_k}\right)$	(27)
				END FOR		

Fig. 4. Non-ordinary state-based peridynamics (NOSB PD) with isotropic finite deformation algorithm sequence where i denotes the particle number, j denotes the neighbouring particles and k denotes the degree of freedom number.

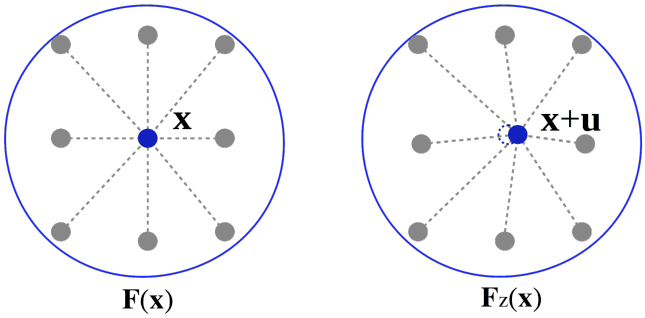

Fig. 5. An illustration of zero-energy modes where $\mathbf{F}(\mathbf{x}) = \mathbf{F}_z(\mathbf{x})$.

particle $\mathbf{x}$ with a circular horizon R which is given a further displacement as shown in Fig. 5, resulting in an additional vector $\mathbf{u}$ while the displacement of other particles are constrained and a new deformation vector state is then

$$\underline{\mathbf{Y}}_z\langle\boldsymbol{\xi}\rangle = \underline{\mathbf{Y}}\langle\boldsymbol{\xi}\rangle - \mathbf{u}, \tag{35}$$

and thus the new deformation gradient $\mathbf{F}_z(\mathbf{x})$ is calculated based on Eq. (16) as

$$\mathbf{F}_z(\mathbf{x}) = \mathbf{F}(\mathbf{x}) - \mathbf{u} \otimes \left(\int_R \omega\langle\boldsymbol{\xi}\rangle \boldsymbol{\xi} dV_{\boldsymbol{\xi}} \right) \mathbf{B}(\mathbf{x})^{-1}. \tag{36}$$

With the assumption of a circular neighbourhood R and a regular lattice of particles, the integration term on the right hand side of Eq. (36) will vanish, and thus $\mathbf{F}_z(\mathbf{x}) = \mathbf{F}(\mathbf{x})$. This shows that the additional displacement of particle $\mathbf{x}$ does not introduce additional deformation into the calculation of the deformation gradient. The presence of zero-energy modes affects the deformation and therefore, various methods have been proposed in order to alleviate this problem.

Breitenfeld et al. [10] introduced two approaches to deal with this problem with supplementary forces. The first approach introduces a supplementary term as a function of relative displacement between particles in the bond whereas in the second approach, the additional force state arising is calculated based on the average of the relative displacement states of all the particles in its horizon. Littlewood [26] developed an additional force term based on penalty term approach. The penalty force was proportional to the difference between the actual position of a particle in the deformed configuration and tends to drive particles toward smooth deformations. However, if the penalty value is too large, the supplementary force will dominate the solution [10] and thus lead to lower accuracy. A stabilised displacement field approach introduced by Wu and Ren eliminated the requirement of the coefficient calculation for the supplementary force however, the oscillation problem still exists in the strain and stress fields [13]. Recently, an attempt has been made by

Silling to eliminate the zero-energy modes by adding a term to the corresponding strain energy density [37], considering the root of the problem as a material rather than a numerical instability, where introduction of an additional term to the force vector state is given by $\underline{\mathbf{T}}_z\langle\boldsymbol{\xi}\rangle$ where

$$\underline{\mathbf{T}}\langle\boldsymbol{\xi}\rangle = \omega(|\boldsymbol{\xi}|)[\sigma^0(\mathbf{F})]^T \cdot \mathbf{B}(\mathbf{x}) \cdot \boldsymbol{\xi} + \underline{\mathbf{T}}_z\langle\boldsymbol{\xi}\rangle. \tag{37}$$

An additional stabilisation term is added to the PD force vector defined as

$$\underline{\mathbf{T}}_z\langle\boldsymbol{\xi}\rangle = \frac{GC}{\omega_0}\underline{\mathbf{z}}(\boldsymbol{\xi}), \tag{38}$$

in which G is a stabilisation parameter whose value will be explored in the numerical examples. It should be noted that parameter, G should be a constant positive number of the order of 1 [37] and C is the nominal micromodulus, stated in [23] as

$$C = \frac{12k'}{\pi h \delta^4}, \tag{39}$$

for 2D problems in which k' is

$$k' = \begin{cases} \frac{E}{2(1-\nu)} & \text{plane stress} \\ \frac{E}{2(1-\nu-2\nu^2)} & \text{plane strain.} \end{cases} \tag{40}$$

For the 2D case, h is the out of plane thickness and ω_0 is the integration of the weighting function in the neighbourhood

$$\omega_0 = \int_R \omega(|\boldsymbol{\xi}|)dV_j, \tag{41}$$

where V_j is the volume of neighbouring particles in the reference configuration. The remaining term, $\underline{\mathbf{z}}(\boldsymbol{\xi})$ is defined in [37] as

$$\underline{\mathbf{z}}(\boldsymbol{\xi}) = \underline{\mathbf{Y}}(\boldsymbol{\xi}) - \mathbf{F}\boldsymbol{\xi}, \tag{42}$$

which represents the state of deformation that deviates from the uniform deformation of the neighbouring particles. It can be seen that the approximate deformation gradient disappears, when the non-uniform part

is included in its approximation of a deformation state [37]

$$\begin{aligned}\left(\int_R \omega(|\boldsymbol{\xi}|)\underline{\mathbf{z}}(\boldsymbol{\xi})\otimes\boldsymbol{\xi}dV_{\boldsymbol{\xi}}\right)\mathbf{B}^{-1} &= \left(\int_R \omega(|\boldsymbol{\xi}|)\underline{\mathbf{Y}}(\boldsymbol{\xi})-\mathbf{F}\boldsymbol{\xi}(\boldsymbol{\xi})\otimes\boldsymbol{\xi}dV_{\boldsymbol{\xi}}\right)\mathbf{B}^{-1}\\ &= \left(\int_R \omega(|\boldsymbol{\xi}|)\underline{\mathbf{Y}}(\boldsymbol{\xi})\otimes\boldsymbol{\xi}dV_{\boldsymbol{\xi}}\right)\mathbf{B}^{-1}-\mathbf{F}\left(\int_R \omega(|\boldsymbol{\xi}|)\,\boldsymbol{\xi}\otimes\boldsymbol{\xi}dV_{\boldsymbol{\xi}}\right)\mathbf{B}^{-1}\\ &= \mathbf{F}-\mathbf{F}\mathbf{B}\mathbf{B}^{-1}\\ &= 0.\end{aligned} \tag{43}$$

In this paper, we use this stabilised correspondence material model in the numerical examples to alleviate the zero-energy mode problem. With the additional stabilisation term added to the internal force, the new Jacobian can be expressed as

$$\begin{aligned}\mathbf{K} = \sum_{i}^{I_n}\sum_{j=1}^{m}\sum_{k}^{ndof}&\left(\omega_i(|\boldsymbol{\xi}|)\frac{\partial\underline{\mathbf{T}}[\mathbf{x}_i,t]}{\partial\mathbf{u}_k}+\frac{GC}{\omega_0}\left(\frac{\partial\underline{\mathbf{Y}}\langle\mathbf{x}_j-\mathbf{x}_i\rangle}{\partial\mathbf{u}_k}-\frac{\partial\mathbf{F}(\mathbf{x}_i)}{\partial\mathbf{u}_k}(\mathbf{x}_j-\mathbf{x}_i)\right)\right)-\\ &\left(\omega_j(|\boldsymbol{\xi}|)\frac{\partial\underline{\mathbf{T}}[\mathbf{x}_j,t]}{\partial\mathbf{u}_k}+\frac{GC}{\omega_0}\left(\frac{\partial\underline{\mathbf{Y}}\langle\mathbf{x}_i-\mathbf{x}_j\rangle}{\partial\mathbf{u}_k}-\frac{\partial\mathbf{F}(\mathbf{x}_j)}{\partial\mathbf{u}_k}(\mathbf{x}_i-\mathbf{x}_j)\right)\right).\end{aligned} \tag{44}$$

3.4. Boundary conditions

Imposition of essential boundary conditions (BC) in PD is somewhat different than in finite element methods. In this section, we describe the available method on how to imposed Dirichlet and Neumann boundary condition in PD. As a nonlocal theory, within which the integral form of the governing equation is evaluated in the nonlocal boundary region, the nonlocal Dirichlet boundary conditions in PD are imposed through a nonzero volume of fictitious boundary layers. As explained in [44] and based on numerical experiments in [45], the extent of the nonzero volume of fictitious boundary layer, R_d, as illustrated in Fig. 6 is suggested. The size of this fictitious boundary layer is equivalent to the size of the horizon used. Displacement boundary conditions are imposed by assigning constraints to the particles in the fictitious boundary layer. This method is proposed to ensure that the imposed prescribed constraints are precisely reflected within the real material domain. The same method has been applied in [46, 47] for beam problems. In the numerical examples given in this work we assign the given displacement value to particles in the fictitious layer where Dirichlet conditions are imposed.

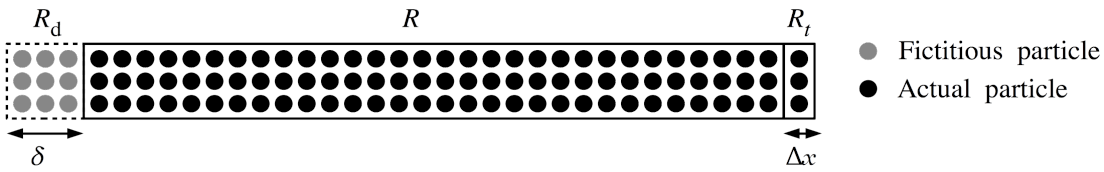

Fig. 6. Application of boundary conditions in peridynamics (PD) beam.

For the quasi-static problems analysed in this paper, an external load can be applied through a layer within the actual region, R_t as shown in Fig. 6 in the form of body loads [44]. The size of this layer equivalent to the size of the particle spacing, Δx.

3.5. Damage criteria

Material damage in PD can be introduced through elimination of interactions (bonds) among particles. Once a bond fails, there is no force sustained in the bond [3] and fracture is modelled via tracking the failure of bonds through the material. In order to specify whether a bond is broken or not, a history-dependent scalar valued function, $\mu(t, \boldsymbol{\eta}, \boldsymbol{\xi})$ is introduced in [3] as

$$\mu(t, \boldsymbol{\eta}, \boldsymbol{\xi}) = \begin{cases} 1 & \text{if } d < d_c, \\ 0 & \text{otherwise,} \end{cases} \tag{45}$$

where d is the damage criteria value and d_c is the critical damage criteria value. Then, based on function $\mu(t, \boldsymbol{\eta}, \boldsymbol{\xi})$, the local damage at $\mathbf{x}$ can be quantified as [3]

$$\varphi(\mathbf{x}, t) = 1 - \frac{\int_R \mu(t, \boldsymbol{\eta}, \boldsymbol{\xi}) dV_{\mathbf{x}'}}{\int_R dV_{\mathbf{x}'}}. \tag{46}$$

The local damage ranges from 0 to 1. If the local damage of a particle is 0, all the interactions associated with the particle are intact, while a local damage of 1 means all the interactions associated with the particle have been eliminated (fully-broken/damaged material). The simplest damage criterion available in the literature is based on the critical bond stretch [48]. This damage criterion had been widely used in BB PD and has been applied in OSB PD and NOSB PD [19, 49]. In terms of the critical bond stretch, it is assumed that when the stretch, s, between two particles, $\mathbf{x}$ and $\mathbf{x}'$, exceeds its critical stretch value, s_{cr}, failure occurs. The stretch between particles $\mathbf{x}$ and $\mathbf{x}'$ is defined as

$$s(t, \boldsymbol{\eta}, \boldsymbol{\xi}) = \frac{\|\eta + \xi\| - \|\xi\|}{\|\xi\|}. \tag{47}$$

3.6. Damage model

Crack begins to initiate when the bond stretch exceeds the critical bond stretch and the influence of this bond on other bonds within the corresponding horizon is removed. However, in order to ensure optimum convergence of the global equilibrium equations, instead of vanishing the influence of bond immediately, a pragmatic approach is to specify a degradation function in the interaction of the bond as the bond stretch increases. A term, T_s is proposed to be added to the force vector-state where

$$T_s = \begin{cases} 1 & \text{if } s < s_{min}, \\ \frac{1}{2}\left(1 - \tanh(\frac{\beta(s_{min}+s_{cr}-2s)}{s_{min}-s_{cr}})\right) & \text{if } s_{min} \leqslant s < s_{cr}, \\ 0 & \text{otherwise.} \end{cases} \tag{48}$$

s_{min} is a value between 0 to s_{cr} and β is a positive constant value to control the rate of degradation in the bond interaction, as shown in Fig. 7. In this paper $\beta = 3$ is used and the new stabilised force vector-state is given by

$$\underline{\mathbf{T}}\langle\boldsymbol{\xi}\rangle = \omega(|\boldsymbol{\xi}|)[\sigma^0(\mathbf{F})]^T \mathbf{B}\,(\mathbf{x})\,\boldsymbol{\xi}\,T_s + \underline{\mathbf{T}}_z\omega(|\boldsymbol{\xi}|)\,T_s. \tag{49}$$

In order to control stability in the simulation, no bonds can completely fail during the equilibrium NR iterations. The bonds are removed after equilibrium has been found and the contribution of the broken bonds to the global stiffness matrix has to be removed. This is to stop oscillations occurring within the NR procedure due to the load redistribution as bonds are removed from the analysis - we have a smooth variation from intact to failed via equal Eq. (48). With the additional softening term added to the internal force, the Jacobian can be expressed as

$$\begin{aligned} \mathbf{K} = \sum_{i}^{I_n}\sum_{j=1}^{m}\sum_{k}^{ndof}\Bigg(&\omega_i(|\boldsymbol{\xi}|)\frac{\partial\underline{\mathbf{T}}[\mathbf{x}_i]}{\partial\mathbf{u}_k}T_s[\mathbf{x}_i] + \omega_i(|\boldsymbol{\xi}|)\frac{\partial T_s[\mathbf{x}_i]}{\partial\mathbf{u}_k}\underline{\mathbf{T}}[\mathbf{x}_i]\Bigg) \\ &-\Bigg(\omega_j(|\boldsymbol{\xi}|)\frac{\partial\underline{\mathbf{T}}[\mathbf{x}_j]}{\partial\mathbf{u}_k}T_s[\mathbf{x}_j] + \omega_i(|\boldsymbol{\xi}|)\frac{\partial T_s[\mathbf{x}_j]}{\partial\mathbf{u}_k}\underline{\mathbf{T}}[\mathbf{x}_j]\Bigg), \end{aligned} \tag{50}$$

and with the stabilisation term, the analytical expression of the new Jacobian is as follows

$$\mathbf{K} = \sum_{i}^{I_n} \sum_{j=1}^{m} \sum_{k}^{ndof} \Bigg(\Big(\omega_i(|\boldsymbol{\xi}|) \frac{\partial \underline{\mathbf{T}}[\mathbf{x}_i]}{\partial \mathbf{u}_k} T_s[\mathbf{x}_i] + \omega_i(|\boldsymbol{\xi}|) \frac{\partial T_s[\mathbf{x}_i]}{\partial \mathbf{u}_k} \underline{\mathbf{T}}[\mathbf{x}_i] \Big) + \Big(T_s[\mathbf{x}_i] \frac{GC}{\omega_0} \Big(\frac{\partial \underline{\mathbf{Y}} \langle \mathbf{x}_j - \mathbf{x}_i \rangle}{\partial \mathbf{u}_k} - \frac{\partial \mathbf{F}(\mathbf{x}_i)}{\partial \mathbf{u}_k} (\mathbf{x}_j - \mathbf{x}_i) \Big) + \underline{\mathbf{T}}_z[\mathbf{x}_i] \omega(|\boldsymbol{\xi}|) \frac{\partial T_s[\mathbf{x}_i]}{\partial \mathbf{u}_k} \Big) \Bigg) - \Bigg(\Big(\omega_j(|\boldsymbol{\xi}|) \frac{\partial \underline{\mathbf{T}}[\mathbf{x}_j]}{\partial \mathbf{u}_k} T_s[\mathbf{x}_j] + \omega_i(|\boldsymbol{\xi}|) \frac{\partial T_s[\mathbf{x}_j]}{\partial \mathbf{u}_k} \underline{\mathbf{T}}[\mathbf{x}_j] \Big) + \Big(T_s[\mathbf{x}_j] \frac{GC}{\omega_0} \Big(\frac{\partial \underline{\mathbf{Y}} \langle \mathbf{x}_i - \mathbf{x}_j \rangle}{\partial \mathbf{u}_k} - \frac{\partial \mathbf{F}(\mathbf{x}_j)}{\partial \mathbf{u}_k} (\mathbf{x}_i - \mathbf{x}_j) \Big) + \underline{\mathbf{T}}_z[\mathbf{x}_j] \omega(|\boldsymbol{\xi}|) \frac{\partial T_s[\mathbf{x}_j]}{\partial \mathbf{u}_k} \Big) \Bigg). \tag{51}$$

The derivative of the softening term with respect to the displacement can be expressed as

$$\frac{\partial T_s[\mathbf{x}_i]}{\partial \mathbf{u}_k} = \frac{\partial T_s}{\partial q} \frac{\partial q}{\partial n} \frac{\partial n}{\partial s} \frac{\partial s}{\partial \|\eta + \xi\|} \frac{\partial \|\eta + \xi\|}{\partial \mathbf{u}_k}, \tag{52}$$

where

$$T_s = \frac{1}{2}(q), \quad q = 1 - \tanh(n) \quad \text{and} \quad n = \frac{\beta(s_{min} + s_{cr} - 2s)}{s_{min} - s_{cr}}, \tag{53}$$

and

$$\frac{\partial T_s}{\partial q} = \frac{1}{2}, \quad \frac{\partial q}{\partial n} = \tanh^2(n-1), \quad \frac{\partial n}{\partial s} = \frac{-2\beta}{s_{min} - s_{cr}} \quad \text{and} \quad \frac{\partial s}{\partial \|\eta + \xi\|} = \frac{1}{\|\xi\|}. \tag{54}$$

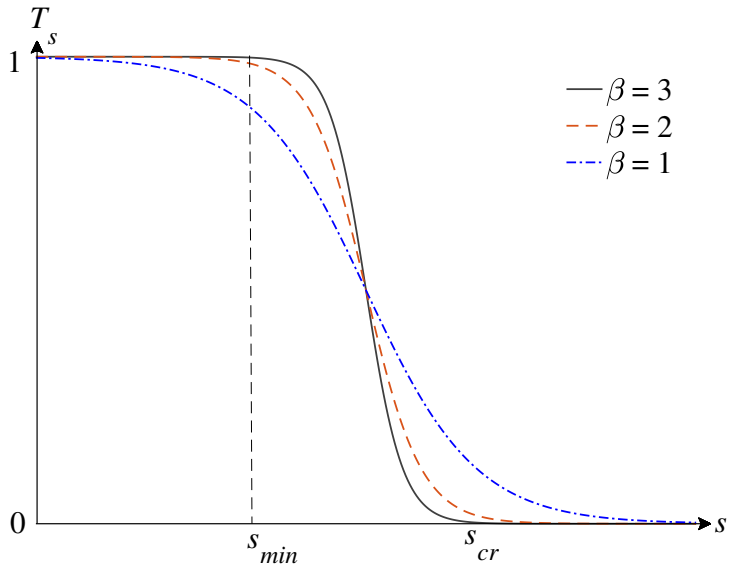

Fig. 7. Scalar function to control the decrease of the bond force, T_s.

The details of this implicit NOSB PD algorithm are given in the flowchart as shown in Fig. 8. As shown, the following procedure is followed:

1. PD simulation starts from initialisation (parameter, mesh generation, interactions search, and boundary conditions).
2. Identify s_{min} and s value.
3. Determine T_{s} and calculate the new force vector-state based, $\underline{\mathbf{T}}\langle\boldsymbol{\xi}\rangle$.
4. The equilibrium equation is solved with iterative update of the modified Jacobian as in Eq. (51).
5. Bonds are allowed to fail after the convergence criterion is attained before applying the next load increment.

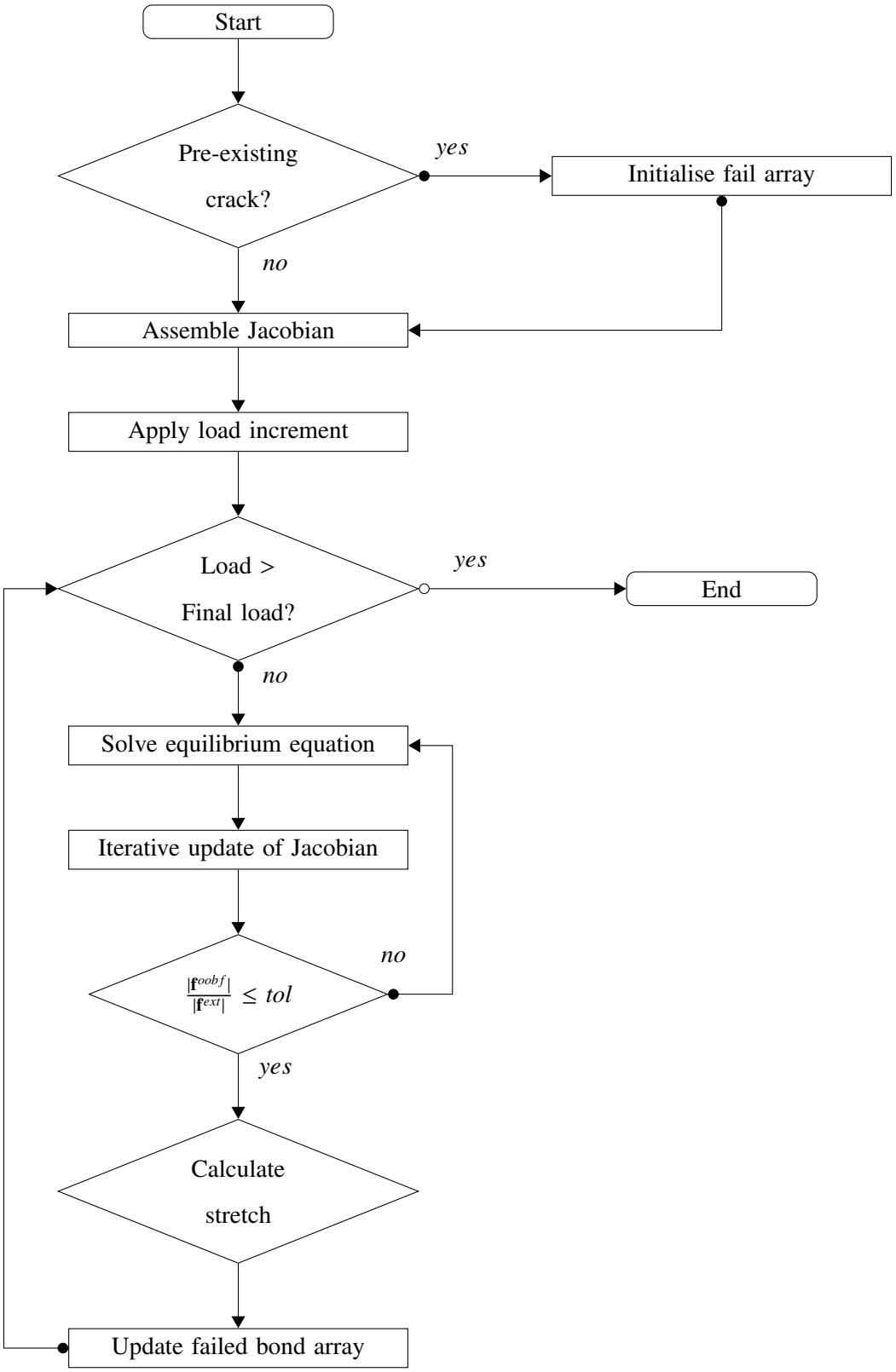

Fig. 8. Flowchart of the NOSB PD implicit algorithm with material failure.

4. Numerical Examples

Five examples are presented here to demonstrate the proposed stabilised implicit NOSB PD formulation. The first example comprises a square plate under hydrostatic extension and is used to demonstrate the effect of the stabilisation parameter, G. The second and third examples apply the stabilised model to a clamped and simply-supported beams respectively and the fourth example models the very large deformation of a cantilever beam subjected to a vertical load at its free end. Finally, the fracture propagation paths are predicted for a rectangular plate with a hole.

4.1. Hydrostatic extension

The first example is a 2D square plate under hydrostatic extension. In the analysis a plane strain condition is assumed in the third direction. The square plate had an initial length of $l_0 = 1$ m, shown in Fig. 9a and was fixed at the middle particle. The material model was isotropic linear elasticity with a Young's modulus of $E = 1.2$ MPa, and a Poisson's ratio of $\nu = 0.2$. The plate was uniformly discretised into 625 particles (arranged in a 25×25 regular grid) with horizon size of $\delta = 1.015\Delta x$, $\delta = 2.015\Delta x$ and $\delta = 3.015\Delta x$. A total force of 5000 kN/m^2 was applied at each side of the plate in a single loadstep and the imposed displacement boundary conditions are shown in Fig. 10. The final configuration is shown in Fig. 9b for the case of $\delta = 2.015\Delta x$ and $G = 1$, clearly demonstrating finite deformation.

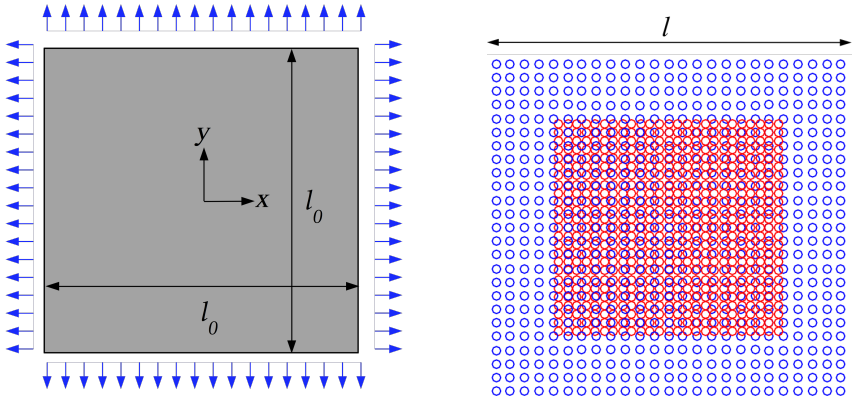

Fig. 9. Hydrostatic extension: (a) initial configuration and (b) initial (red) and final (blue) configurations with $\delta = 2.015\Delta x$ and $G = 1$.

The analytical deformation gradient and logarithmic strain for this problem are

$$[\mathbf{F}] = \begin{bmatrix} l/l_0 & 0 \\ 0 & l/l_0 \end{bmatrix} \quad \text{and} \quad [\boldsymbol{\epsilon}] = \ln \begin{bmatrix} l/l_0 & 0 \\ 0 & l/l_0 \end{bmatrix}. \tag{55}$$

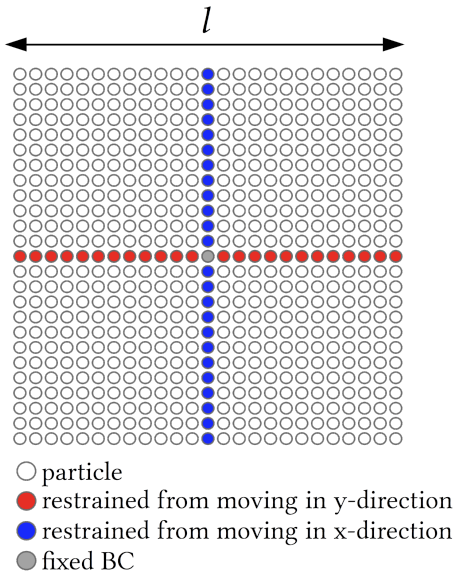

Fig. 10. Hydrostatic expansion: displacement BC.

From the analytical solution given in Eq. (55), the displacement normal to each side of the plate was calculated to be 0.30667 m (l = 1.61334 m). The displacement error, e_u was given as

$$e_u = \frac{1}{V} \sum_{i}^{I_n} \left(\frac{|\mathbf{u}_p - \mathbf{u}|}{|\mathbf{u}|} V_i \right), \tag{56}$$

where $\mathbf{u}$ is the displacement calculated from the analytical solution. Fig. 11 shows the dependence of the displacement error based on G for different horizon sizes, δ and normalised particle spacing Δx/L. It is clear that the PD solution's error decreases with increasing G values, achieving a minimum error before it rises for higher coefficient values, where the solution is controlled by the correction time. The larger horizon size increase the effects of the zero-energy modes in that a larger stabilisation parameter is needed to minimise the error. Particular values of stabilisation parameter can affect the error. For $\delta = 1.015\Delta x$, the G values only need to be as large as 0.01 in order to obtain the minimum error. In addition, the results shown in Fig. 11 illustrate a larger relative error of displacement as the particle spacing becomes larger. Fig. 12 shows the convergence rate for simulations which varies between 0.43 and 0.91 depending on the number of particles

and the horizon size. It can be clearly seen that varying the number of particles and horizon sizes has an impact on the path to the solutions to this problem.

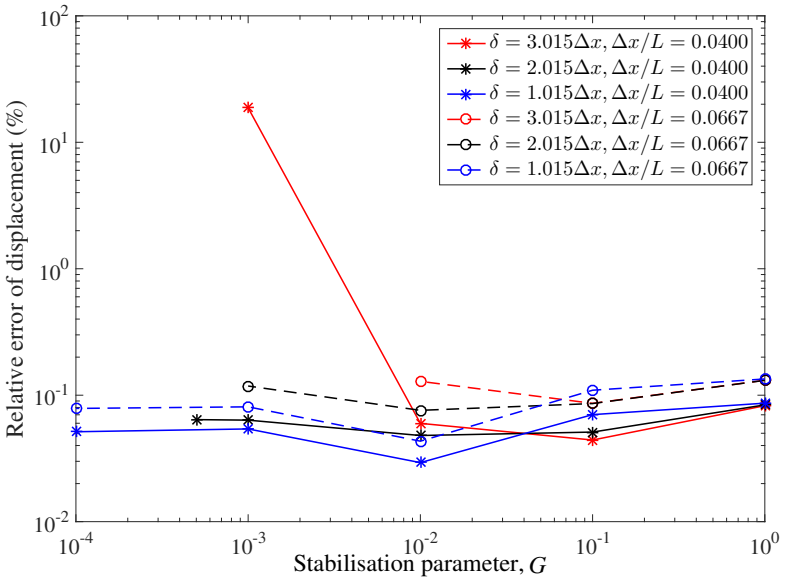

Fig. 11. Hydrostatic expansion: relative displacement error with G for different δ and Δx/L .

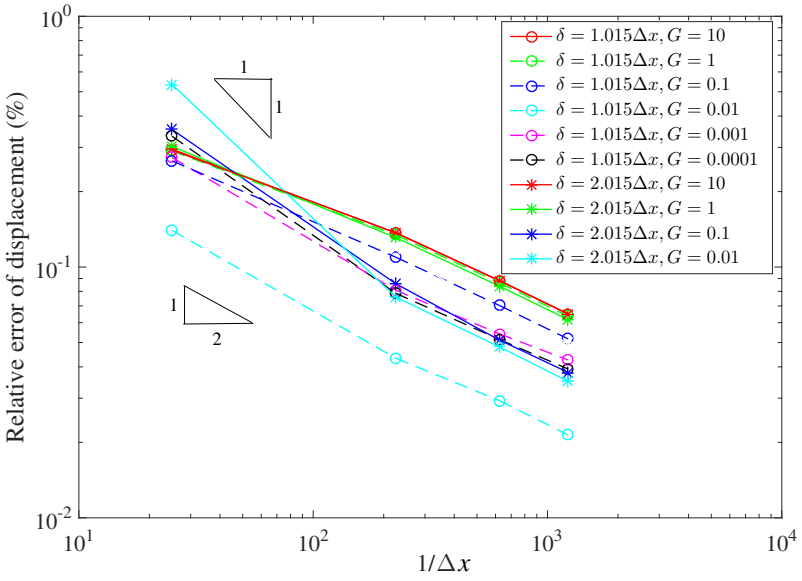

Fig. 12. Hydrostatic expansion: convergence with $\delta = 1.015\Delta x$ and $\delta = 2.015\Delta x$.

4.2. Clamped slender beam subjected to a uniform transverse pressure

The second problem considered was the behaviour of a slender beam subjected to a uniform transverse pressure of p = 276 kPa applied in 10 loadsteps. The beam domain at the beginning had a length, L of 254 mm and a depth, d_0 of 5.08 mm, Young's modulus of $E = 68.95$ GPa and Poisson's ratio of $\nu = 0.25$. Due to symmetry, only half of the beam was analysed and uniformly discretised into two different particle discretisations. To further quantify the effectiveness, three different horizon sizes of $\delta = 1.015\Delta x$, $\delta = 2.015\Delta x$ and $\delta = 3.015\Delta x$ and different values of the stabilisation parameter were used. In order to implement a clamped boundary condition, a fictitious boundary layer was introduced outside the actual material domain at the boundary region where the size of the layer was equivalent to the horizon size and displacement boundary conditions were imposed through the fictitious boundary layer. As shown in Fig. 13, the left hand end of the beam was pinned at the fictitious boundary region along the beam's mid-axis, thus not allowing the structure to move in both x and y-direction and roller boundary conditions applied to other particles along the left hand fictitious region, allowing the structure to move only in the y-direction in this location. Roller boundary conditions were also imposed along the centreline line of symmetry, as shown by the blue particles on the right hand end of the discretised beam in Fig. 13. A uniform transverse pressure was applied to all the particles on the top surface with the same load and a tolerance of 1×10^{-10} was used on the global normalised out of balance force for unstabilised ($G = 0$) and stabilised ($G > 0$) correspondence material.

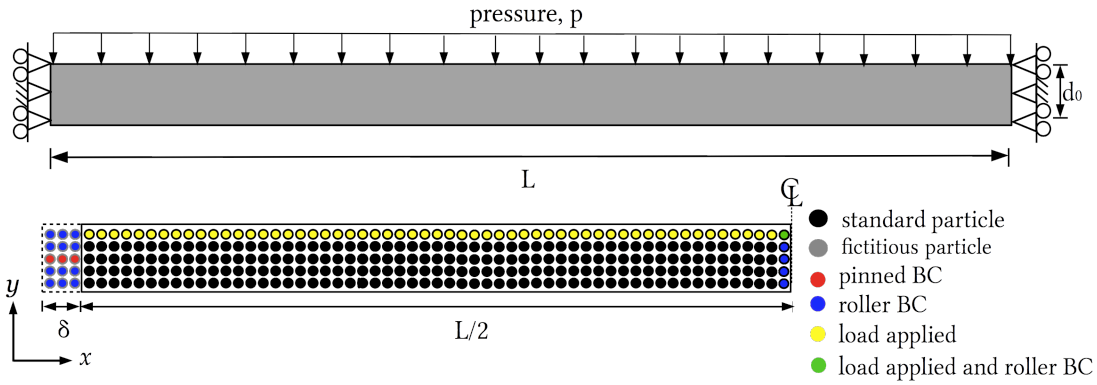

Fig. 13. Clamped slender beam subjected to uniform pressure, p.

In Figs. 14 and 15, the final normalised vertical displacement of the material is compared against the analytical solution of the same problem [50] for two different particle discretisations: 3×75 particles and 5×125 particles with different horizon sizes and different values of G. For a given particle spacing, the

displacement obtained shows larger departures from the analytical solution in the absence of zero-energy control as the horizon size increases, as shown in Figs. 14 and 15, while the smallest horizon size of one particle spacing used in this problem, minimises the effects of zero-energy modes.

The relative displacement errors, e_u are given for different particle discretisations and different horizon sizes for unstabilised material in Table 1. As can be seen, there are significant differences ($e_u = 6.678 \times 10^0$ for $\delta = 1.015\Delta x$, $e_u = 2.733 \times 10^1$ for $\delta = 2.015\Delta x$ and $e_u = 6.380 \times 10^1$ for $\delta = 3.015\Delta x$) between the three horizon sizes with 3×75 particles. It is seen that as the horizon size increases, the errors increase. These numerical results are in general agreement with observation published in [10, 18], in which it had been demonstrated that the resulting axial displacement and stress show significant instabilities and errors as the horizon size increases in the absence of zero-energy control. This behaviour could be due to larger horizon sizes, where a larger number of bonds are connected to each particle which leads to an increase in the non-uniform part of the deformation state, with the missing role of the centre particle. Hence, it is expected that larger stabilisation term may need to be added to the force state in order to be effective at suppressing zero-energy indicating that G must be adjusted based on the horizon size. However, continuing to increase the value of G results in an eventual increase of stiffness, thus artificially affecting the displacement as seen in both Figs. 14 and 15. It is found that with horizon size of one particle spacings, variations of the particles in vertical direction had little influence on the results.

Comparing the results in Figs. 14 and 15, it can be seen that with the finer particle discretisation in Fig. 15, the error for an unstabilised material ($G = 0$) is smaller than those in Fig. 14 for all horizon sizes. Therefore using simulations with smaller particle spacings is a possible way to decrease the zero-energy mode oscillation although it significantly reduces the computational efficiency. Clearly, the discretisation scheme (i.e the particle arrangement) plays an important role in selecting the optimum value of G and we can infer that NOSB PD analysis results are mesh dependent.

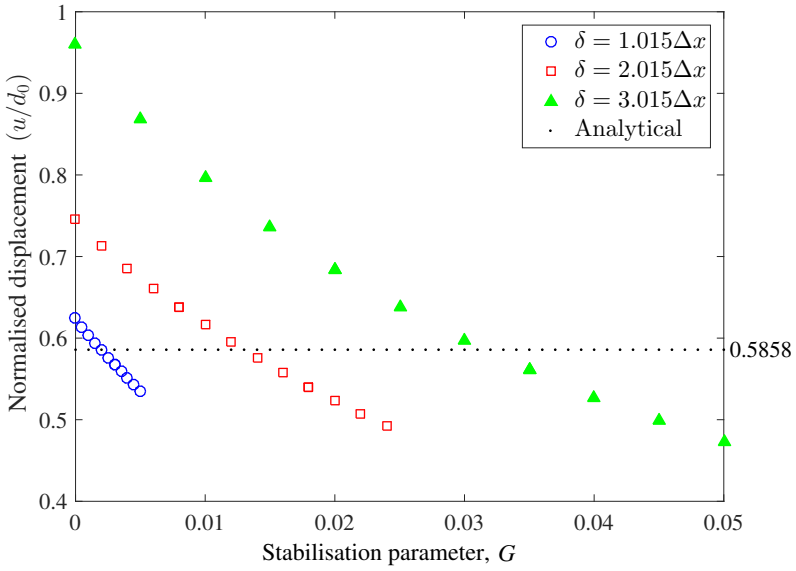

Fig. 14. Clamped beam: normalised vertical displacement with changing G values and horizon sizes with 3×75 particles.

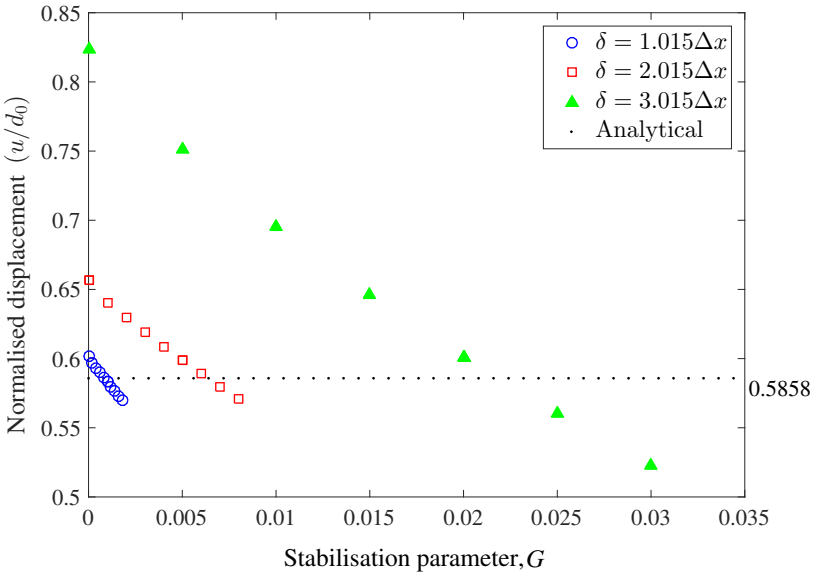

Fig. 15. Clamped beam: normalised vertical displacement with changing G values and horizon sizes with 5×125 particles.

Figure Fig. 16 shows the error against computational time for the implicit approach developed in this paper alongside that of an explicit implementation using dynamic relaxation to achieve a pseudo static

result. In this case the horizon size was set to $\delta = 1.015\Delta x$, $G = 0$ and the particle discretisation was varied. The errors and timings are for a uniform pressure of p = 276 kPa applied over 10 loadsteps. The results show that for a given discretisation, both methods predict the same response, with the same relative displacement error. The figure also show that the implicit time integration has a significantly reduced computational time. This is due to the number of iterations required by the explicit algorithm to achieve a pseudo static, or steady state, response. All of the analysis were conducted using MATLAB 2015b on an Intel Core i5, CPU 2.40 GHz.

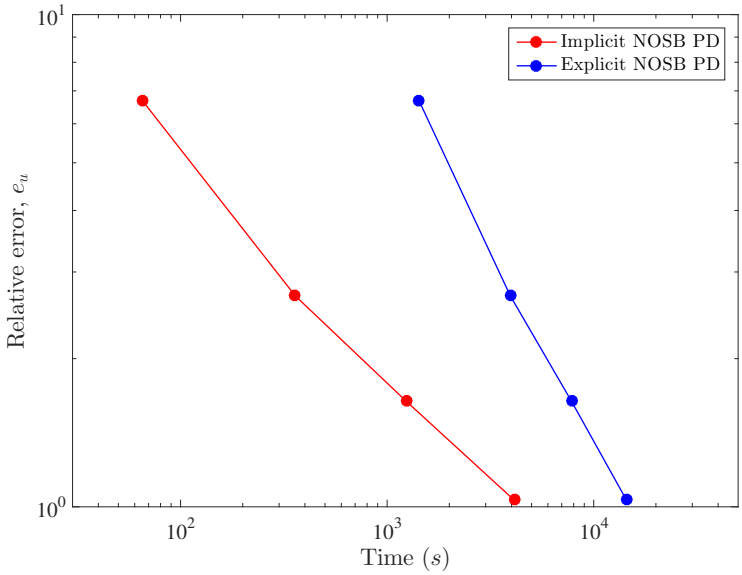

Fig. 16. Clamped beam: displacement error versus time for implicit and explicit NOSB PD.

In Fig. 17, the maximum normalised vertical displacement of the material is compared against the analytical solution of the same problem with 3×75 particles and three different horizon sizes with an "optimum" stabilisation parameter, $G = 0.002$ with $\delta = 1.015\Delta x$, $G = 0.013$ with $\delta = 2.015\Delta x$ and $G = 0.031$ with $\delta = 3.015\Delta x$. The results using the NOSB PD are presented alongside the analytical solution of Molstad [50]. In all cases excellent agreement is seen between the NOSB PD normalised vertical displacement with the analytical result.

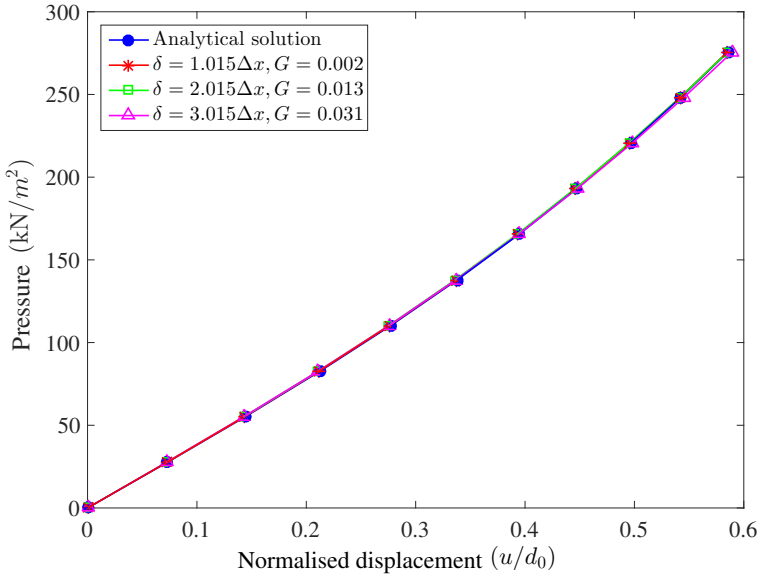

Fig. 17. Clamped beam: normalised midpoint vertical displacements with 3×75 particles and different δ.

Table 1. Clamped beam: Relative displacement error with different particle discretisations and different horizon sizes for $G = 0$.

Particles discretisation	Horizon size, δ	Relative displacement error (%)
3×75	$1.015\Delta x$	6.678×10^0
	$2.015\Delta x$	2.733×10^1
	$3.015\Delta x$	6.380×10^1
5×125	$1.015\Delta x$	2.683×10^0
	$2.015\Delta x$	1.216×10^1
	$3.015\Delta x$	4.050×10^1
7×175	$1.015\Delta x$	1.638×10^0
9×225	$1.015\Delta x$	1.032×10^0

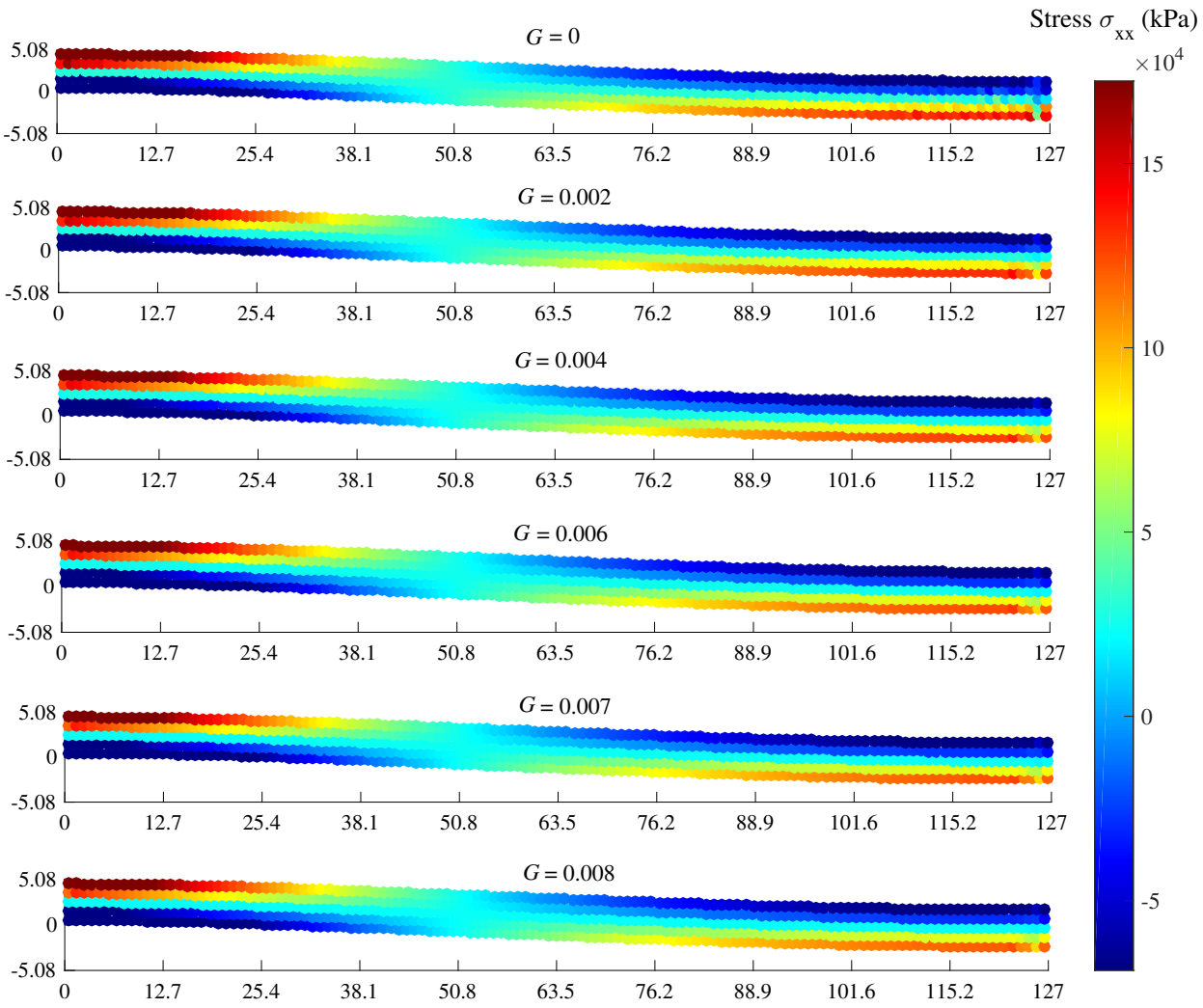

Fig. 18. Clamped beam: stress contour, σ_{xx} for p = 276 kPa, $\delta = 2.015\Delta x$ with 5×125 particles with different G

Contours of normal stress component, σ_{xx}, and the deformed shape of the beam (x-axis and y-axis: mm) corresponding to the external load for p = 276 GPa, $\delta = 2.015\Delta x$ and 5×125 particles for the clamped slender beam using $G = 0$, 0.002, 0.004, 0.006, 0.007 and 0.008 are compared in Fig. 18. The plots show that, without stabilisation, NOSB PD shows instabilities, evident for instance in the top plot, where colour corresponds to stress magnitude in kPa. The absence of the zero-energy mode control leads to significant oscillation in the stress field, which is most obvious near the support and the region experiencing larger displacements. The stabilisation method proposed in [37] effectively suppresses the zero-energy modes as G is increased up to $G = 0.006$, resulting in a stabilised stress field. However, continuing to increase the value of G results in a domination of the stabilisation force density over the PD force density which

subsequently results in an increase of stiffness. Table 2 presents the global Newton-Raphson (NR) residual for the final 5 steps with 3×75 particles and $\delta = 3.015\Delta x$ and a global tolerance of 1×10^{-10}. Notable in Table 2 is that the data shows near quadratic convergence behaviour and a maximum number of iterations of 4, indicating a correct implementation.

Table 2. Clamped beam: Newton-Raphson residuals showing near-quadratic convergence ($tol = 1 \times 10^{-10}$) with $\delta = 3.015\Delta x$ and $G = 0.031$.

Step	6	7	8	9	10
Iteration 1	4.781×10^{-2}	3.680×10^{-2}	2.890×10^{-2}	2.313×10^{-2}	1.871×10^{-2}
Iteration 2	4.799×10^{-5}	3.805×10^{-5}	2.920×10^{-5}	2.206×10^{-5}	1.659×10^{-5}
Iteration 3	2.332×10^{-9}	1.341×10^{-9}	7.413×10^{-10}	4.036×10^{-10}	2.201×10^{-10}
Iteration 4	3.532×10^{-12}	2.686×10^{-12}	2.965×10^{-12}	2.434×10^{-12}	2.626×10^{-12}

4.3. Simply-supported slender beam

A beam with the same material and geometric properties as the clamped slender beam in the example above but having simply-supported ends was next analysed. The same particle discretisations were used, however the boundary conditions at the support were appropriately modified. As in the previous example, the fictitious boundary layer, of equivalent size to the horizon was introduced outside the actual material domain at the boundary region and displacement boundary conditions were imposed through this layer. To model the simply-supported edge, only one particle at the left hand fictitious region of the middle surface was prevented from having in-plane displacement, allowing free rotation of the remainder of the end as shown in Fig. 19. The problem was analysed using a loading increment of 27.6 kPa, applied in 10 loadsteps to a maximum loading of 276 kPa. Due to symmetry, only half of the beam was analysed and uniformly discretised into two different particle discretisations with three different horizon sizes.

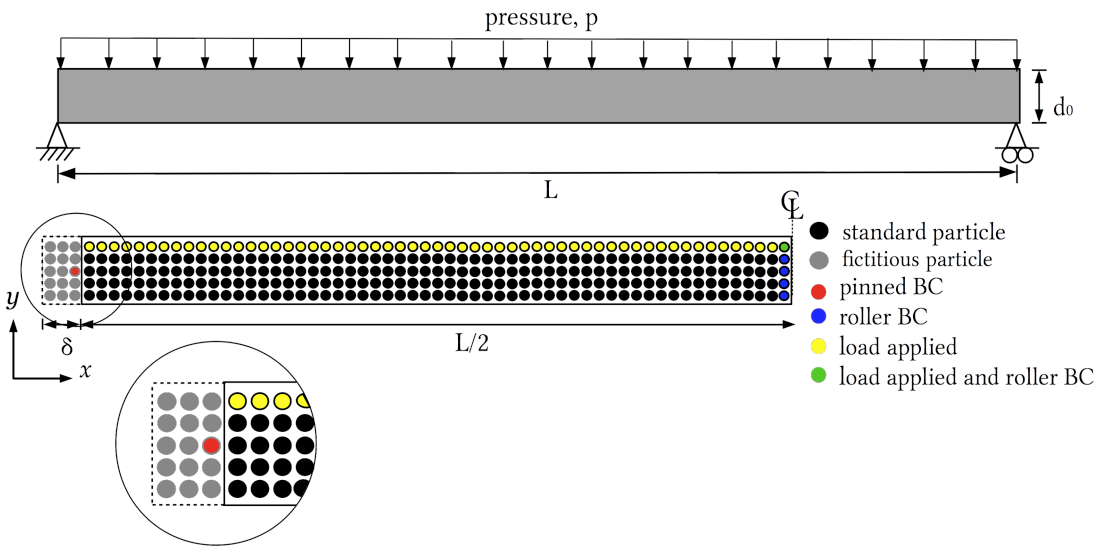

Fig. 19. Simply-supported slender beam subjected to uniform transverse pressure.

The conclusions reached for the previous example are again supported by the results from this example in that the impact of zero-energy modes for larger horizon size results in larger displacements for a given particle spacing in the absence of additional stabilisation. The final normalised vertical displacement is compared in Figs. 20 and 21 against the analytical result for two different particle discretisations, i.e. 3×75 particles and 5×125 particles, with different horizon sizes and different value of the stabilisation parameter, G. The agreement between analytical and numerical solutions reduces as the horizon size increases, however the small horizon size of one particle spacing used in this problem tends itself to minimise the effect of the zero-energy modes. It is to be expected that a larger stabilisation parameter value would need to be added to the original PD force state for a problem with a larger horizon size in order to be effective at suppressing zero-energy modes. Since the PD formulations is nonlocal, this finding, while preliminary, predicts that the maximum accuracy will be achieved only for the horizon size of zero. The optimum value of G for larger horizon sizes is

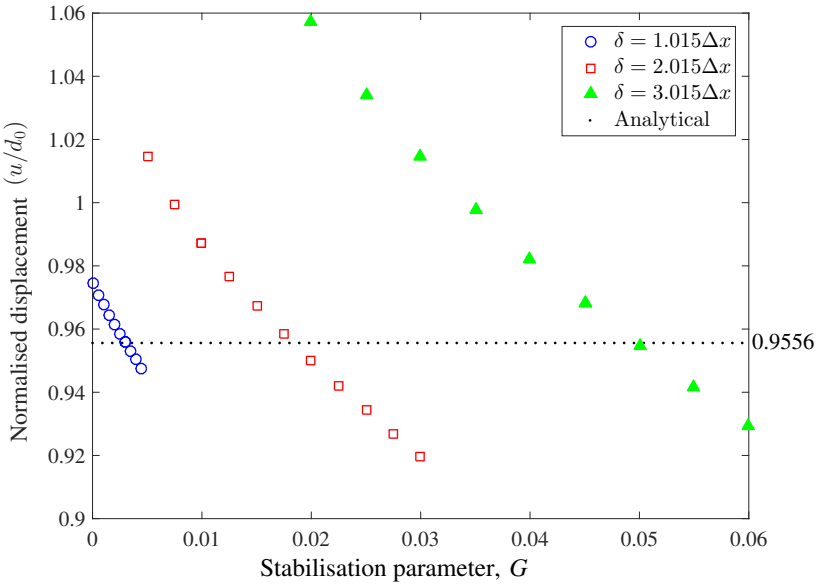

Fig. 20. Simply-supported beam: normalised vertical displacement with changing G values and horizon sizes with 3 × 75 particles.

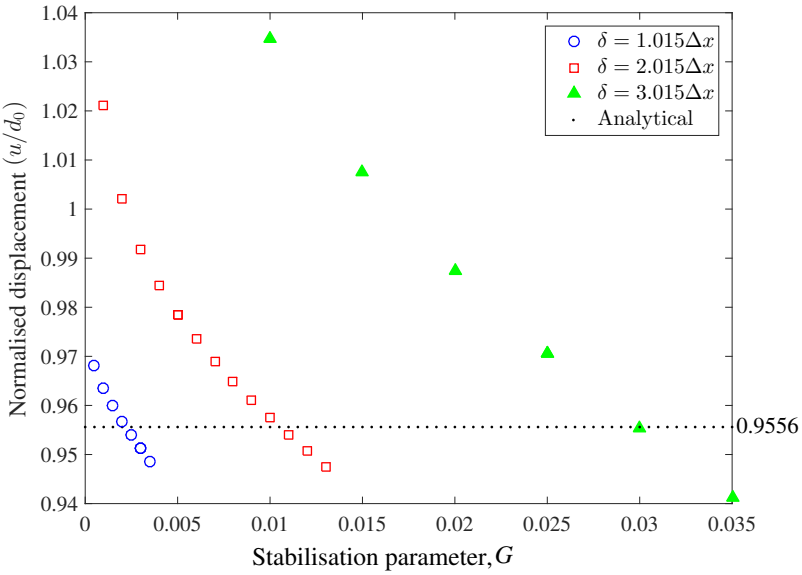

Fig. 21. Simply-supported beam: normalised vertical displacement with changing G values and horizon sizes with 5 × 125 particles.

shown to be larger in order to provide enough stiffness for stability. However, continuing to increase the

value of G once again results in an increase of non-realistic stiffness, and hence artificially reduced displacements as seen in both Figs. 20 and 21. In Fig. 22, the pressure versus normalised displacement response is compared against the analytical solution. The response is shown with three different horizon sizes, with stabilisation parameters of $G = 0$ with $\delta = 1.015\Delta x$, $G = 0.05$ with $\delta = 2.015\Delta x$ and $G = 0.315$ with $\delta = 3.015\Delta x$. The analytical solution given by Molstad [50] is also shown. It can be clearly seen that the normalised vertical displacements agree well with the analytical result for all the horizon sizes.

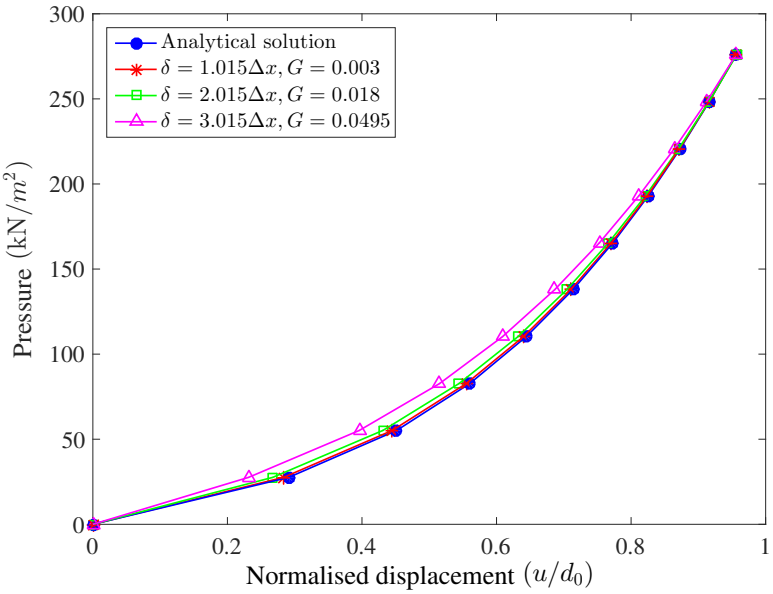

Fig. 22. Simply-supported beam: normalised vertical end with 3×75 particles.

Contours of normal stress component, σ_{xx}, and the deformed shape of the beam (x-axis and y-axis: mm) corresponding to the total external load of p = 276 kPa, with $\delta = 1.015\Delta x$ and a 5×125 particle distribution for the simply-supported slender beam problem are shown in Fig. 23. Once again it is clear that NOSB PD solutions exhibit instabilities, indicating the necessity of zero-energy mode control. The absence of the zero-energy mode control leads to significant oscillations in the stress field. Increasing the value of G from 0 to 0.01 significantly reduces the stress oscillation leading to a more realistic stress profile. The zero-energy modes are still evident closer to the supported end if $G < 0.01$. However, continuing to increase G results in the stabilisation force density dominating the original PD force density which then results in an increase in stiffness and a consequent drop in displacement. Table 3 gives the global Newton-Raphson (NR) residual for loadsteps 6 to 10 in this problem, with $G = 0.02$ and $\delta = 2.015\Delta x$. The global tolerance

was 1×10^{-10} and the data presented in the table shows quadratic (or near quadratic) convergence of the global out of balance force, demonstrating a correct implementation of the algorithmic consistent tangent for finite deformation elasticity.

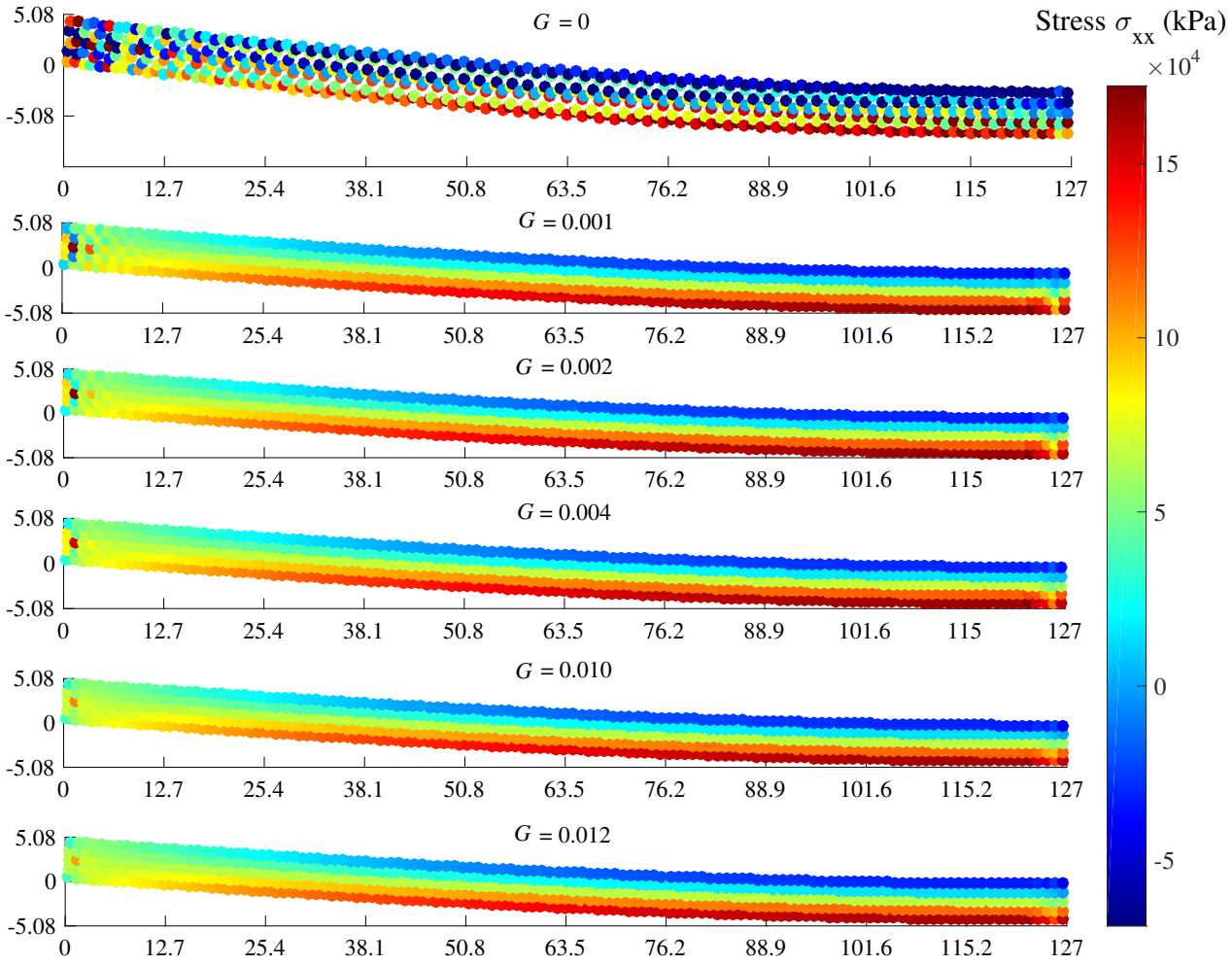

Fig. 23. Simply-supported beam: stress contour, σ_{xx}, for p = 276 kPa, $\delta = 2.015\Delta x$, 5×125 particles with different G.

Table 3. Simply-supported beam: Newton-Raphson residuals showing near-quadratic convergence ($tol = 1 \times 10^{-10}$) with $\delta = 2.015\Delta x$ and $G = 0.02$.

Step	6	7	8	9	10
Iteration 1	6.120×10^{-2}	4.421×10^{-2}	3.070×10^{-2}	2.342×10^{-2}	1.842×10^{-2}
Iteration 2	2.610×10^{-4}	1.285×10^{-4}	7.000×10^{-5}	4.113×10^{-5}	2.568×10^{-5}
Iteration 3	5.343×10^{-8}	1.279×10^{-8}	3.780×10^{-9}	1.309×10^{-9}	5.126×10^{-10}
Iteration 4	7.758×10^{-12}	6.316×10^{-12}	5.661×10^{-12}	5.383×10^{-12}	5.357×10^{-12}

4.4. Cantilever beam

The fourth example tested was of a deep elastic cantilever beam, fixed at one end and subjected to a vertical mid-height particle load on its free end. The beam has a length, L of 10 m, depth, d_0 of 1 m, and is uniformly discretised with 5×50 particles. Three values of horizon radius, $\delta = 1.015\Delta x$, $\delta = 2.015\Delta x$ and $\delta = 3.015\Delta x$ were used in this problem. The material properties were Young's modulus, $E = 12$ MPa and Poisson's ratio, $\nu = 0.2$. The beam was pinned at the fictitious boundary region at the mid-axis in both directions and roller boundary conditions applied to other particles along the left hand fictitious region, allowing the structure to move only in the y-direction as shown in Fig. 24. A vertical load of 100 kN was applied in 10 loadsteps with a tolerance of $1{\times}10^{-10}$ used on the global normalised out of balance force. The loads are applied through a layer of actual particles on the right hand region at the mid-axis, as shown in Fig. 24.

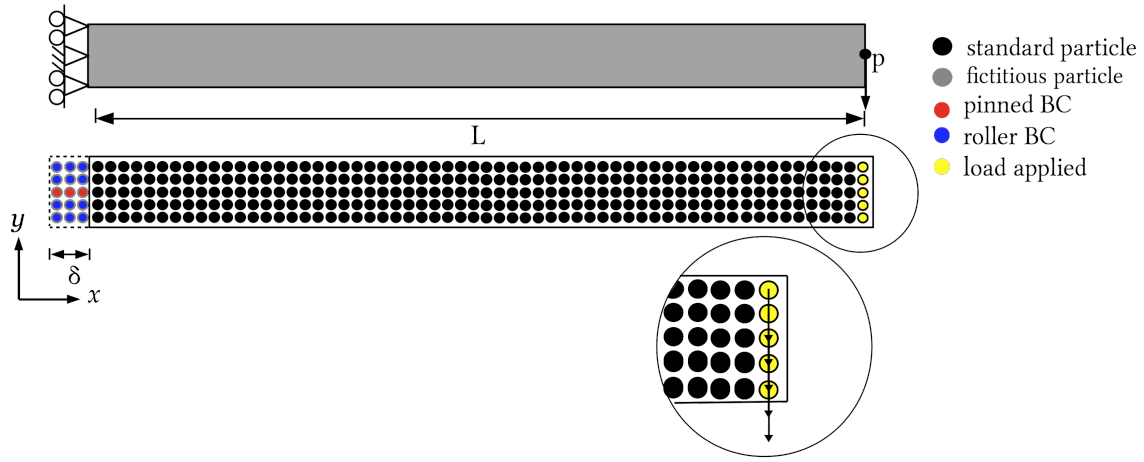

Fig. 24. Cantilever beam subjected to vertical mid-side load.

Fig. 25 compares the normalised displacement, at the end of the beam for different values of δ and G with the analytical solution [50] corresponding to the external load of 10 kN. As shown in the figure, for the unstabilised material, a significant difference in terms of normalised displacement ($e_u = 0.302$ with $\delta = 1.015\Delta x$, $e_u = 0.342$ with $\delta = 2.015\Delta x$ and $e_u = 0.529$ with $\delta = 3.015\Delta x$) is evident between those three horizon sizes. From Fig. 25, we can also see that increasing G from an initial value of 0 visibly affects the normalised displacements.

In Fig. 26, the load-deflection results predicted by the NOSB PD are compared against the analytical solution for the same problem [50] with three different horizon sizes and optimum stabilisation parameters, i.e. $G = 0$ with $\delta = 1.015\Delta x$, $G = 0.05$ with $\delta = 2.015\Delta x$ and $G = 0.315$ with $\delta = 3.015\Delta x$. Fig. 26 shows there to be good agreement with the corresponding analytical solution with the optimum stabilisation parameter. It can be clearly seen that errors are small with smallest horizon values, $\delta = 1.015\Delta x$ without the addition of the stabilised term to NOSB PD. This agrees with the results published in [23] where the zero-energy mode is not significant in local horizon ($\delta = 1\Delta x$) compared to the larger neighbourhoods. Thus, a very small value of G is needed to eliminate any zero-energy mode for problems with horizon $\delta = 1.015\Delta x$.

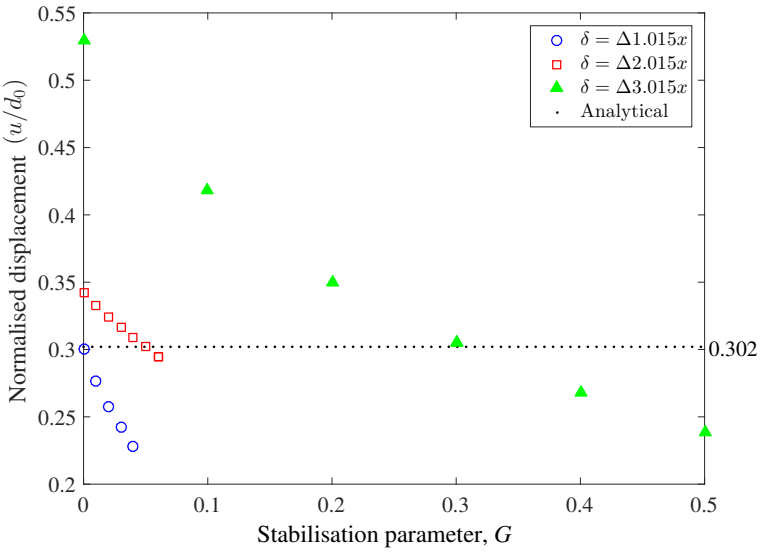

Fig. 25. Cantilever beam: normalised vertical displacement with changing G and horizon sizes with with 5×50 particles.

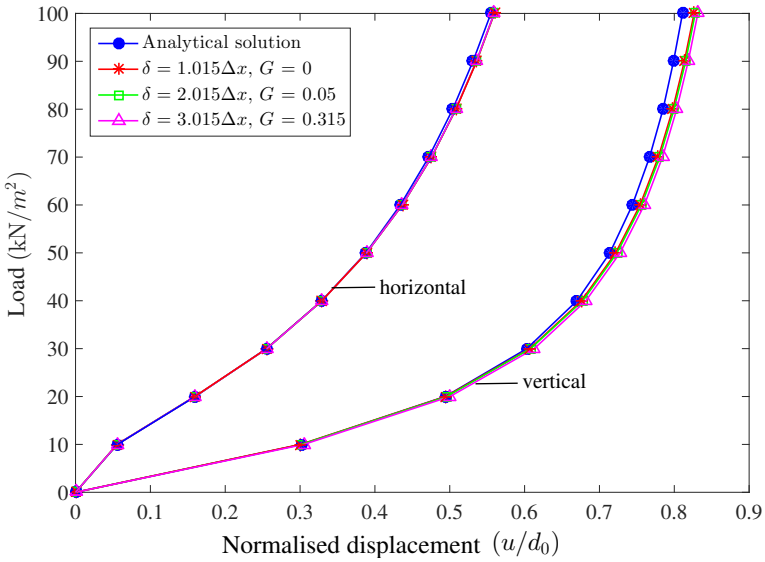

Fig. 26. Cantilever beam: normalised vertical and horizontal displacement at the midpoint of the free end with 5×50 particles.

Contour plots of the three stress components and the deformed shape for the fully loaded cantilever are shown in Fig. 27. These are plotted on the final deformed configuration showing the very large deformations modelled. The stabilisation method proposed in [37] effectively suppresses the zero-energy modes with the increased value of G, resulting in a stabilised stress field. However, for this problem, the method fails to converge with horizon sizes of $\delta = 2.015\Delta x$ when $G < 0.05$. Table 4 shows the convergence for the final 5 load steps of the Newton-Raphson process in this case. It can be seen that the Newton-Raphson algorithm needs more load steps to find the correct path, which then reaches asymptotic quadratic convergence.

Table 4. Cantilever beam: Newton-Raphson residuals showing near-quadratic convergence ($tol = 1 \times 10^{-10}$) with $\delta = 2.015\Delta x$ and $G = 0.05$.

Step	6	7	8	9	10
Iteration 1	2.746×10^{-1}	1.513×10^{-1}	9.050×10^{-2}	5.792×10^{-2}	3.921×10^{-2}
Iteration 2	6.012×10^{-1}	6.251×10^{-4}	4.244×10^{-4}	2.790×10^{-4}	1.773×10^{-4}
Iteration 3	1.419×10^{-3}	3.054×10^{-4}	6.681×10^{-5}	1.526×10^{-5}	3.758×10^{-6}
Iteration 4	3.705×10^{-8}	1.838×10^{-9}	1.679×10^{-10}	1.863×10^{-11}	1.861×10^{-12}
Iteration 5	2.420×10^{-13}	7.773×10^{-14}	8.187×10^{-14}	–	–

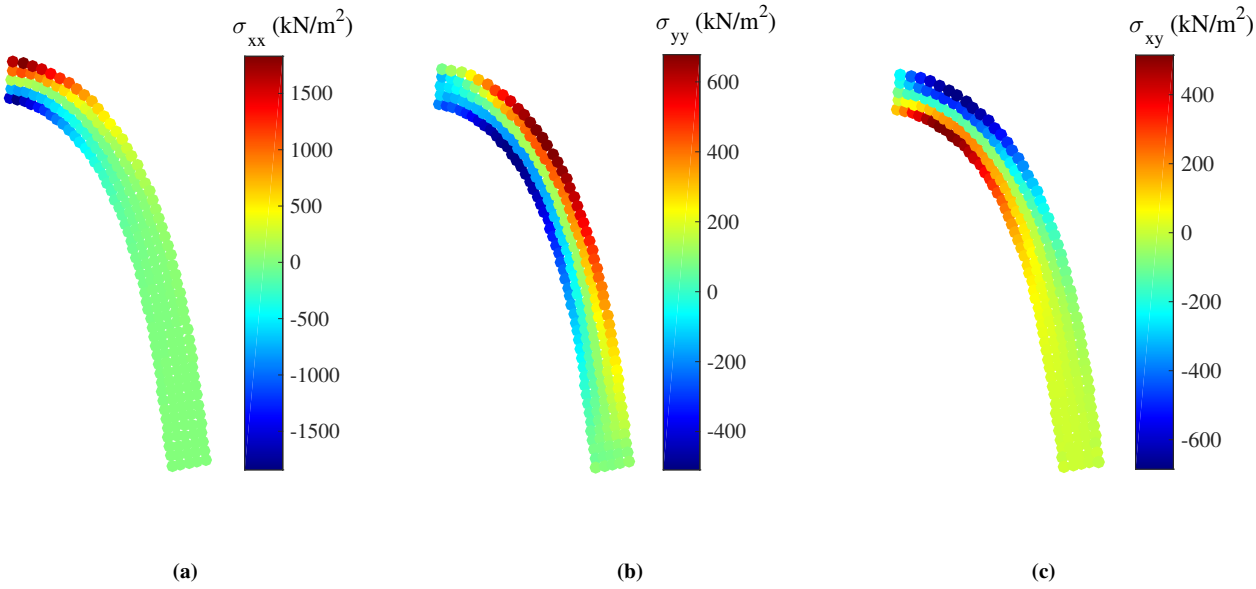

Fig. 27. Cantilever beam: stress distribution for p = 100 kN (a) σ_{xx}, (b) σ_{yy} and (c) σ_{xy} with $\delta = 2.015\Delta x$ and $G = 0.05$.

4.5. Plate with a hole

The final problem considered is the behaviour of a rectangular plate with a circular hole in the centre. The left and right ends of the plate were subjected to a horizontal displacement in opposite directions of 1×10^4 mm in 15 loadsteps as illustrated in Fig. 28. Layers of fictitious boundary particles introduced outside the actual material domain at the boundary region where the size of the layer was equivalent to the horizon size and the Dirichlet BC were imposed through the fictitious boundary layer.

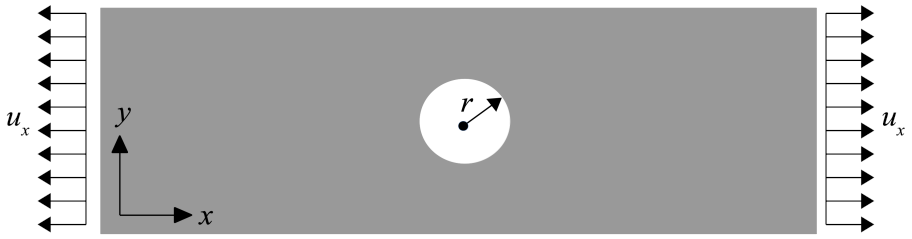

Fig. 28. Plate with circular hole: geometry.

The plate initially had a length, L of 150 mm and a width, W of 50 mm with radius of hole, r of 10 mm, Young's modulus of $E = 210$ GPa and Poisson's ratio of $\nu = 0.33$. The analysis assumes plane strain

conditions. Horizon radius, $\delta = 3.015\Delta x$ and particle discretisations of 30×10 particles were used. The displacement plots in x directions without material damage with 30×10 particles and without stabilisation is shown in Fig. 29, resulting in an unstabilised displacement field. The same problem was analysed with $G = 0.01$ and the results are shown in Fig. 30. Increasing the value of G in this problem from 0 to 0.01 leading to a more realistic displacement profile.

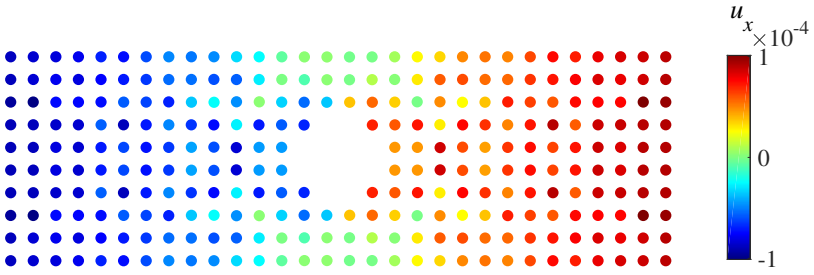

Fig. 29. Plate with circular hole: horizontal displacement plots (NOSB PD) when failure is not allowed with 30×10 particles and $G = 0$.

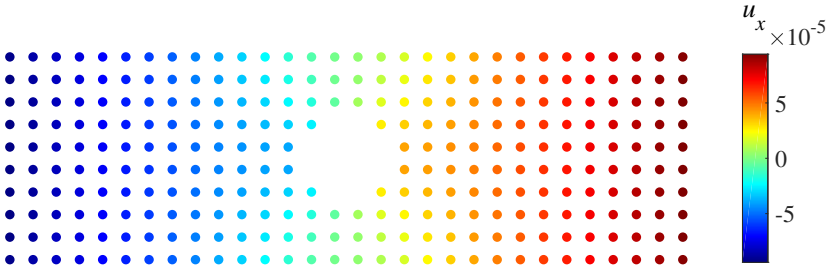

Fig. 30. Plate with a circular hole: horizontal displacement plots (NOSB PD) when failure is not allowed with 30×10 particles with $G = 0.01$.

Damage is now incorporated and the critical stretch failure criterion is adopted, with a critical stretch $s_{cr} = 0.002$ and $s_{min} = 0.0015$. As illustrated in Fig. 31, damage is plotted with $G = 0.01$ at the end of the analysis. It can be seen that the modelling predicts a wide damage area in terms of crack shape.

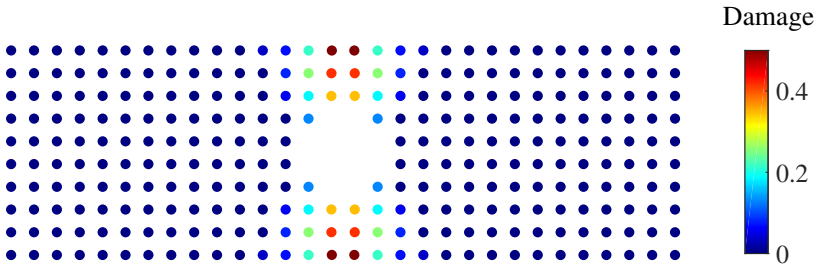

Fig. 31. Plate with a circular hole: damage with 30×10 particles and $G = 0.01$ at the end of the analysis.

A finer grid spacing is now used for the same problem with 150×50 particles. Additionally, FEM analysis was used to verify the accuracy of the results obtained by the proposed PD model. The variation of horizontal displacement along the central axes when damage was not allowed is shown in Fig. 32. The determination of the stabilisation parameter, G needs to be done before the damage is considered. From Fig. 32, it can be seen that increasing G from an initial value of 0 visibly affects the displacements in the x-direction. The stabilisation method is demonstrated to be effective on suppressing zero-energy modes as G is increased up to $G = 0.001$.

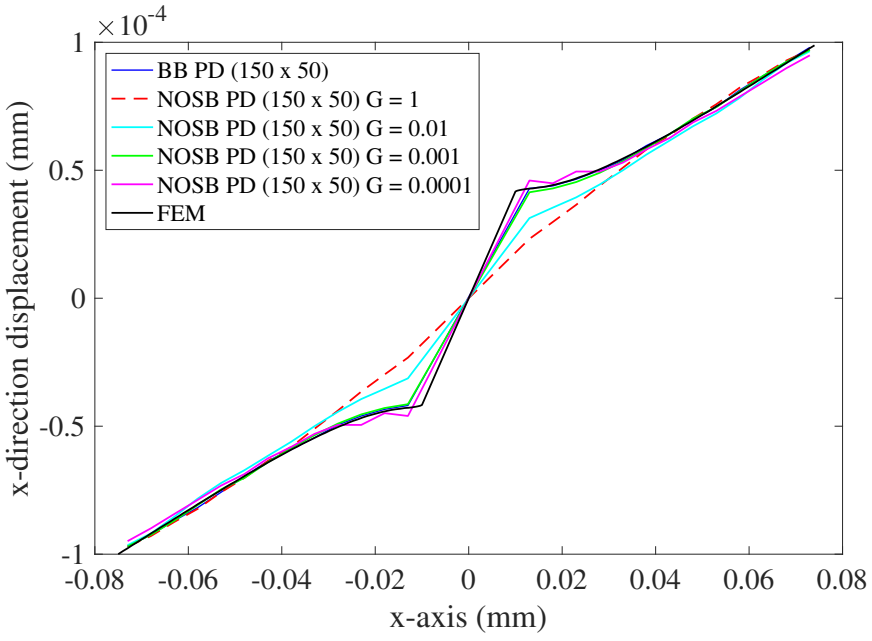

Fig. 32. Plate with circular hole: variation of horizontal displacement along the central axes when failure is not allowed with 150×50 particles.

However, continuing to increase the value of G results in a domination of the stabilisation force density over the PD force density which subsequently results in the increase of stiffness. Fig. 33 shows the displacement plots without damage with $G = 0.001$, and the damage plots when failure is allowed is shown in Fig. 34. As expected, the cracks are initiated from the hole boundary and propagates towards the edges of the plate.

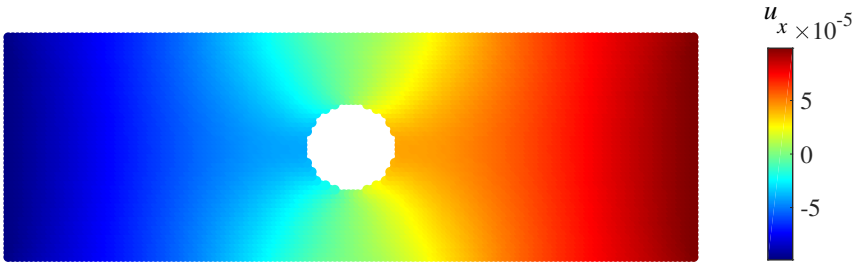

Fig. 33. Plate with a circular hole: horizontal displacement plots (NOSB PD) when failure is allowed with 150×50 particles and $G = 0.001$.

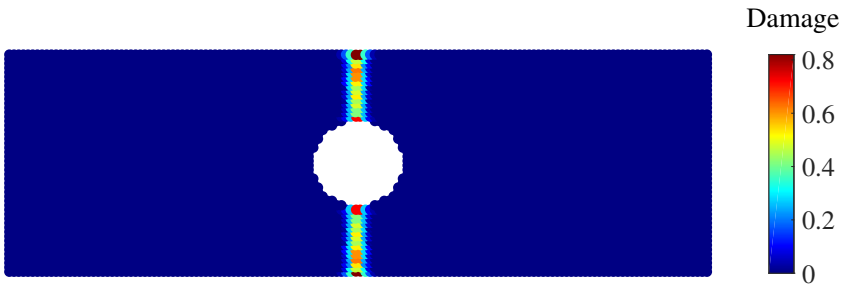

Fig. 34. Plate with a circular hole: damage plots (NOSB PD) when failure is allowed with 150×50 particles and $G = 0.001$.

5. Conclusion

This paper has presented for the first time a development of non-ordinary state-based peridynamics (NOSB PD) for finite deformation with an implicit time integration scheme since the existing literature on NOSB PD focuses particularly on explicit schemes. The key contribution of this paper is the construction of the Jacobian matrix based on the analytical expression of the equation of motion of NOSB PD. Within this, a proper implementation of the Jacobian was confirmed by the convergence rate of the global residual force in the various examples presented. The proposed formulation appears also to be the first study to

demonstrate the modelling of 2D material focusing on quasi-static problems with finite strains.

It has been shown that NOSB PD is quite capable of simulating complex problems involving materials undergoing large deformation with finite deformation theory. Interestingly, this paper has been one of the first attempts to include modification of the correspondence material model proposed by Silling [37] in eliminating zero-energy modes for finite deformation analysis. The derivative of this stabilisation term with respect to displacement has been included in the formulation of the Jacobian matrix for the first time. Similar to other numerical methods, NOSB PD suffers from instability induced by zero-energy modes. Therefore, introducing an additional stabilisation term to the force density results in an eventual increase of the material stiffness and a stabilised stress field. A progressive damage model has been implemented for the first time in an implicit NOSB PD framework.

Five numerical examples are presented to validate the effectiveness of this approach where analytical results exist. Results from these examples show horizon sizes and particle spacing in different problems appear to be related to the optimum value of G. Overall, these results indicate that the NOSB PD simulation becomes mesh dependent in the absence of zero-energy mode control and for a given particle spacing, a smaller horizon size shows greater accuracy with no control on the zero-energy modes. The stabilised correspondence material model allows the proposed boundary condition to be used and bounds for values of the stabilisation parameter G to be assessed to ensure stability. Additionally, it is shown that the value of the optimum stabilisation parameter G used in this paper is a positive constant less than 1, as also been suggested by Silling in [37].

The focus of this paper has been on the development of an implicit framework for large deformation peridynamic analysis. Although the examples presented in this paper are in two-dimensions, the algorithms are general in that they can be applied to one, two and three dimensional analysis. This paper lays the groundwork for NOSB PD future research into a broader range of large deformation problems modelled using NOSB PD. It also provides a starting point for modelling large deformation damage and fracture within an implicit peridynamic setting for pseudo static problems.

6. Acknowledgement

Nur A. Hashim gratefully acknowledges the support from Ministry of Education Malaysia and University of Malaysia Perlis for the funding.

Appendix A. Material tangent modulus

The derivative of the Piola-Kirchhoff with respect to the deformation gradient is given by

$$\begin{aligned} A_{imkn} &= \frac{\partial}{\partial F_{kn}}(\tau_{ip}F^{-T}_{pm}) \\ &= \frac{\partial}{\partial F_{kn}}(\tau_{ip}F^{-1}_{mp}) \\ &= \frac{\partial \tau_{ip}}{\partial F_{kn}}F^{-1}_{mp} + \tau_{ip}\frac{\partial F^{-1}_{mp}}{\partial F_{kn}}, \end{aligned} \tag{A.1}$$

and the derivative of the Kirchhoff stress tensor with respect to the deformation gradient in the first term of the right-hand side of Eq. (A.1) can be shown to be

$$\begin{aligned} M_{ipkn} &= \frac{\partial \tau_{ip}}{\partial F_{kn}} \\ &= \frac{\partial \tau_{ip}}{\partial \epsilon_{ab}}\frac{\partial \epsilon_{ab}}{\partial c_{cd}}\frac{\partial c_{cd}}{\partial F_{kn}} \\ &= \frac{1}{2}\frac{\partial \tau_{ip}}{\partial \epsilon_{ab}}\frac{\partial ln(c_{ab})}{\partial c_{cd}}\frac{\partial c_{cd}}{\partial F_{kn}}, \end{aligned} \tag{A.2}$$

where the derivative of the elastic logarithmic strain tensor with respect to the elastic left Cauchy-Green strain tensor follows as

$$Q_{abcd} = \frac{\partial \epsilon_{ab}}{\partial b_{cd}} = \frac{1}{2}\frac{\partial ln(c_{ab})}{\partial c_{cd}}, \quad \text{where} \quad c_{ab} = F_{ac}F_{bc}. \tag{A.3}$$

Q_{abcd} can be solved as a case of the derivative of symmetric second order isotropic tensor argument (see Miehe [51] for details). Derivative in the second term of the right-hand side of the equation (31) is given by

$$\frac{\partial \tau_{ip}}{\partial \epsilon_{ab}} = D^{e}_{ipab}, \tag{A.4}$$

where the D^{e}_{ipab} must be write in four by four matrix notation . Derivative in the last term of the right-hand side of the Eq. (A.2) is given by

$$\begin{aligned} N_{cdkn} = \frac{\partial c_{cd}}{\partial F_{kn}} &= \frac{\partial F_{cg}F_{dg}}{\partial F_{kn}} \\ &= F_{dg}\frac{\partial F_{cg}}{\partial F_{kn}} + F_{cg}\frac{\partial F_{dg}}{\partial F_{kn}} \\ &= F_{dg}\delta_{kc}\delta_{gn} + F_{cg}\delta_{kd}\delta_{gn} \\ &= F_{dn}\delta_{kc} + F_{cn}\delta_{kd}, \end{aligned} \tag{A.5}$$

where δ_{kc} denotes the Kronecker delta tensor defined by

$$\delta_{kc} = 1 \quad \text{if} \quad k = c, \quad \delta_{kc} = 0 \quad \text{if} \quad k \neq c. \tag{A.6}$$

From the relation for the derivative of the inverse of a tensor given in the literature, the derivative in the last term of the right-hand side of the Eq. (A.1) is given by

$$B_{pmkn} = \Big[\frac{\partial (F^{-1})_{mp}}{\partial F_{kn}}\Big]^T = (-(F^{-1})_{mk}(F^{-1})_{np})^T. \tag{A.7}$$

Substituting Eq. (A.7) into Eq. (A.1) gives

$$A_{imkn} = \frac{\partial \tau_{ip}}{\partial F_{kn}} F^{-1}_{mp} - \tau_{ip} F^{-T}_{mk} F^{-T}_{np}. \tag{A.8}$$

References

[1] S. A. Silling, Reformulation of elasticity theory for discontinuities and long-range forces, Journal of the Mechanics and Physics of Solids. 48 (1) (2000) 175–209. doi:10.1016/S0022-5096(99)00029-0.

[2] E. Madenci, E. Oterkus, Peridynamic Theory and Its Applications, Springer New York, New York, NY, 2014. doi:10.1007/978-1-4614-8465-3.

[3] S. A. Silling, E. Askari, A meshfree method based on the peridynamic model of solid mechanics, Computers and Structures. 83 (17-18) (2005) 1526–1535. doi:10.1016/j.compstruc.2004.11.026.

[4] S. A. Silling, F. Bobaru, Peridynamic modeling of membranes and fibers, International Journal of Non-Linear Mechanics. 40 (2-3) (2005) 395–409. doi:10.1016/j.ijnonlinmec.2004.08.004.

[5] W. Gerstle, N. Sau, S. Silling, Peridynamic modeling of concrete structures, Nuclear Engineering and Design. 237 (12-13) (2007) 1250–1258. doi:10.1016/j.nucengdes.2006.10.002.

[6] B. Kilic, A. Agwai, E. Madenci, Peridynamic theory for progressive damage prediction in center-cracked composite laminates, Composite Structures. 90 (2) (2009) 141–151. doi:10.1016/j.compstruct.2009.02.015.

[7] S. A. Silling, M. Epton, O. Weckner, J. Xu, E. Askari, Peridynamic States and Constitutive Modeling, Journal of Elasticity. 88 (2) (2007) 151–184. doi:10.1007/s10659-007-9125-1.

[8] T. L. Warren, S. A. Silling, A. Askari, O. Weckner, M. A. Epton, J. Xu, A non-ordinary state-based peridynamic method to model solid material deformation and fracture, International Journal of Solids and Structures. 46 (5) (2009) 1186–1195. doi:10.1016/j.ijsolstr.2008.10.029.

[9] J. T. Foster, S. A. Silling, W. W. Chen, Viscoplasticity using peridynamics, International Journal for Numerical Methods in Engineering. 81 (2009) 1242–1258. doi:10.1002/nme.2725.

[10] M. S. Breitenfeld, P. H. Geubelle, O. Weckner, S. A. Silling, Non-ordinary state-based peridynamic analysis of stationary crack problems, Computer Methods in Applied Mechanics and Engineering. 272 (2014) 233–250. doi:10.1016/j.cma.2014.01.002.

[11] J. O'Grady, J. Foster, Peridynamic beams: A non-ordinary, state-based model, International Journal of Solids and Structures. 51 (18) (2014) 3177–3183. doi:10.1016/j.ijsolstr.2014.05.014.

[12] J. O'Grady, J. Foster, Peridynamic plates and flat shells: A non-ordinary, state-based model, International Journal of Solids and Structures. 51 (25-26) (2014) 4572–4579. doi:10.1016/j.ijsolstr.2014.09.003.

[13] C. T. Wu, B. Ren, A stabilized non-ordinary state-based peridynamics for the nonlocal ductile material failure analysis in metal machining process, Computer Methods in Applied Mechanics and Engineering. 291 (2015) 197–215. doi:10.1016/j.cma.2015.03.003.

[14] X. P. Zhou, Y. T. Wang, Numerical simulation of crack propagation and coalescence in pre-cracked rock-like Brazilian disks using the non-ordinary state-based peridynamics, International Journal of Rock Mechanics and Mining Sciences. 89 (October) (2016) 235–249. doi:10.1016/j.ijrmms.2016.09.010.

[15] X. Zhou, Y. Wang, Q. Qian, Numerical simulation of crack curving and branching in brittle materials under dynamic loads using the extended non-ordinary state-based peridynamics, European Journal of Mechanics, A/Solids. 60 (2016) 277–299. doi:10.1016/j.euromechsol.2016.08.009.

[16] J. Amani, E. Oterkus, P. Areias, G. Zi, T. Nguyen-Thoi, T. Rabczuk, A non-ordinary state-based peridynamics formulation for thermoplastic fracture, International Journal of Impact Engineering. 87 (2016) 83–94. doi:10.1016/j.ijimpeng.2015.06.019.

[17] Y. Wang, X. Zhou, X. Xu, Numerical simulation of propagation and coalescence of flaws in rock materials under compressive loads using the extended non-ordinary state-based peridynamics, Engineering Fracture Mechanics. 163 (2016) 248–273. doi:10.1016/j.engfracmech.2016.06.013.

[18] A. Yaghoobi, M. G. Chorzepa, Higher-order approximation to suppress the zero-energy mode in non-ordinary state-based peridynamics, Computers and Structures. 188 (2017) 63–79. doi:10.1016/j.compstruc.2017.03.019.

[19] P. Li, Z. M. Hao, W. Q. Zhen, A stabilized non-ordinary state-based peridynamic model, Computer Methods in Applied Mechanics and Engineering. 339 (2018) 262–280. doi:10.1016/j.cma.2018.05.002.

[20] G. Hattori, J. Trevelyan, W. M. Coombs, A non-ordinary state-based peridynamics framework for anisotropic materials, Computer Methods in Applied Mechanics and Engineering. 339 (2018) 416–442. doi:10.1016/j.cma.2018.05.007.

[21] J. Luo, V. Sundararaghavan, Stress-point method for stabilizing zero-energy modes in non-ordinary state-based peridynamics, International Journal of Solids and Structures. 150 (2018) 197–207. doi:10.1016/j.ijsolstr.2018.06.015.

[22] X. Gu, E. Madenci, Q. Zhang, Revisit of non-ordinary state-based peridynamics, Engineering Fracture Mechanics. 190 (2018) 31–52. doi:10.1016/j.engfracmech.2017.11.039.

[23] C. Nicely, S. Tang, D. Qian, Nonlocal matching boundary conditions for non-ordinary peridynamics with correspondence material model, Computer Methods in Applied Mechanics and Engineering. 338 (2018) 463–490. doi:10.1016/j.cma.2018.04.027.

[24] X. Lai, L. Liu, S. Li, M. Zeleke, Q. Liu, Z. Wang, A non-ordinary state-based peridynamics modeling of fractures in quasi-brittle materials, International Journal of Impact Engineering. 111 (2018) 130–146. doi:10.1016/j.ijimpeng.2017.08.008.

[25] X. Gu, Q. Zhang, D. Huang, Y. Yv, Wave dispersion analysis and simulation method for concrete SHPB test in peridynamics, Engineering Fracture Mechanics. 160 (2016) 124–137. doi:10.1016/j.engfracmech.2016.04.005.

[26] D. J. Littlewood, A Nonlocal Approach to Modeling Crack Nucleation in AA 7075-T651, in: Volume 8: Mechanics of Solids, Structures and Fluids; Vibration, Acoustics and Wave Propagation, ASME, 2011, pp. 567–576. doi:10.1115/IMECE2011-64236.

[27] S. Sun, V. Sundararaghavan, A peridynamic implementation of crystal plasticity, International Journal of Solids and Structures. 51 (19-20) (2014) 3350–3360. doi:10.1016/j.ijsolstr.2014.05.027.

[28] X. Gu, Q. Zhang, E. Madenci, Non-ordinary state-based peridynamic simulation of elastoplastic deformation and dynamic cracking of polycrystal, Engineering Fracture Mechanics 218 (2019) 106568. doi:10.1016/j.engfracmech.2019.106568.

[29] N. Hashim, W. Coombs, G. Hattori, C. Augarde, An implicit implementation of non-ordinary state-based peridynamics., in: Proceedings of the 25th Conference on Computational Mechanics (UKACM 2017), University of Birmingham, Birmingham, 2017, pp. 134–137.
URL http://dro.dur.ac.uk/21985/

[30] F. Bobaru, J. T. Foster, P. H. Geubelle, S. A. Silling, Handbook of peridynamic modeling, CRC press, 2016.

[31] B. Kilic, E. Madenci, An adaptive dynamic relaxation method for quasi-static simulations using the peridynamic theory, Theoretical and Applied Fracture Mechanics. 53 (3) (2010) 194–204. doi:10.1016/j.tafmec.2010.08.001.

[32] W. Liu, J. W. Hong, A coupling approach of discretized peridynamics with finite element method, Computer Methods in Applied Mechanics and Engineering. 245-246 (2012) 163–175. doi:10.1016/j.cma.2012.07.006.

[33] M. D. Brothers, J. T. Foster, H. R. Millwater, A comparison of different methods for calculating tangent-stiffness matrices in a massively parallel computational peridynamics code, Computer Methods in Applied Mechanics and Engineering. 279 (2014) 247–267. doi:10.1016/j.cma.2014.06.034.

[34] D. Huang, G. Lu, P. Qiao, An improved peridynamic approach for quasi-static elastic deformation and brittle fracture analysis, International Journal of Mechanical Sciences. 94-95 (2015) 111–122. doi:10.1016/j.ijmecsci.2015.02.018.

[35] Y. Wang, X. Zhou, Y. Wang, Y. Shou, A 3-D conjugated bond-pair-based peridynamic formulation for initiation and propagation of cracks in brittle solids, International Journal of Solids and Structures. 134 (2018) 89–115. doi:10.1016/j.ijsolstr.2017.10.022.

[36] T. Ni, M. Zaccariotto, Q. Z. Zhu, U. Galvanetto, Static solution of crack propagation problems in Peridynamics, Computer Methods in Applied Mechanics and Engineering 346 (2019) 126–151. doi:10.1016/j.cma.2018.11.028.
URL https://doi.org/10.1016/j.cma.2018.11.028

[37] S. A. Silling, Stability of peridynamic correspondence material models and their particle discretizations, Computer Methods in Applied Mechanics and Engineering. 322 (2017) 42–57. doi:10.1016/j.cma.2017.03.043.

[38] M. R. Tupek, R. Radovitzky, An extended constitutive correspondence formulation of peridynamics based on nonlinear bond-strain measures, Journal of the Mechanics and Physics of Solids. 65 (1) (2014) 82–92. doi:10.1016/j.jmps.2013.12.012.

[39] D. P. Flanagan, T. Belytschko, A uniform strain hexahedron and quadrilateral with orthogonal hourglass control, International Journal for Numerical Methods in Engineering. 17 (5) (1981) 679–706. doi:10.1002/nme.1620170504.

[40] H. Chen, Bond-associated deformation gradients for peridynamic correspondence model, Mechanics Research Communications. 90 (2018) 34–41. doi:10.1016/j.mechrescom.2018.04.004.

[41] H. Chen, B. W. Spencer, Peridynamic bond-associated correspondence model: Stability and convergence properties, International Journal for Numerical Methods in Engineering 117 (6) (2019) 713–727. doi:10.1002/nme.5973.

[42] L. Anand, On H. Hencky's Approximate Strain-Energy Function for Moderate Deformations, Journal of Applied Mechanics. 46 (1) (1979) 78. doi:10.1115/1.3424532.

[43] P. Deuflhard, Newton Methods for Nonlinear Problems: Affine Invariance and Adaptive Algorithms, Springer Publishing Company, Incorporated, 2011.

[44] S. Oterkus, Peridynamics for the solution of multiphysics problems, Ph.D. thesis, The University of Arizona (2015).

[45] R. W. Macek, S. A. Silling, Peridynamics via finite element analysis, Finite Elements in Analysis and Design. 43 (15) (2007) 1169–1178. doi:10.1016/j.finel.2007.08.012.

[46] C. Diyaroglu, E. Oterkus, S. Oterkus, E. Madenci, Peridynamics for bending of beams and plates with transverse shear deformation, International Journal of Solids and Structures. 69-70 (2015) 152–168. doi:10.1016/j.ijsolstr.2015.04.040.

[47] Z. Yang, E. Oterkus, C. Tien, Implementation of peridynamic beam and plate formulations, Continuum Mechanics and Thermodynamics. 31 (1) (2019) 301–315. doi:10.1007/s00161-018-0684-0.

[48] E. Madenci, K. Colavito, N. Phan, Peridynamics for unguided crack growth prediction under mixed-mode loading, Engineering Fracture Mechanics. 167 (2016) 34–44. doi:10.1016/j.engfracmech.2016.04.009.

[49] Y. Zhang, P. Qiao, Peridynamic Simulation of Two-dimensional Axisymmetric Pull-out Tests, International Journal of Solids and Structures (xxxx). doi:10.1016/j.ijsolstr.2019.03.014.
URL https://doi.org/10.1016/j.ijsolstr.2019.03.014

[50] T. K. Molstad, Finite Deformation Analysis using the Finite Element Method, Ph.D. thesis, The University of British Columbia (1977). doi:10.14288/1.0062686.

[51] C. Miehe, Comparison of two algorithms for the computation of fourth-order isotropic tensor functions, Computers & Structures. 66 (1) (1998) 37–43. doi:10.1016/S0045-7949(97)00073-4.